Understanding the Performance of an Unstructured-Mesh Global Shallow Water Model on Kinetic Energy Spectra and Nonlinear Vorticity Dynamics

Lei WANG[1], Yi ZHANG[1*], Jian LI[1], Zhuang LIU[2], and Yihui ZHOU[3]

1 *State Key Laboratory of Severe Weather*, *Chinese Academy of Meteorological Sciences*, *China Meteorological Administration*, *Beijing* 100081
2 *National Supercomputing Center in Wuxi*, *Wuxi* 214011
3 *State Key Laboratory of Numerical Modeling for Atmospheric Sciences and Geophysical Fluid Dynamics*, *Institute of Atmospheric Physics*, *Chinese Academy of Sciences*, *Beijing* 100029

(Received January 28, 2019; in final form July 15, 2019)

ABSTRACT

A strategy for evaluating a global shallow water model based on aspects of kinetic energy spectra and nonlinear vorticity dynamics is proposed in this study. The kinetic energy spectra and nonlinear vorticity dynamics of a recently developed global shallow water model on an unstructured mesh are evaluated in comparison with the benchmark solutions from a global high-resolution spectral model. The results show that the kinetic energy spectra, the rotational and divergent components, the stationary and transient components, and the nonlinear spectral fluxes of the developed shallow water model agree well with those generated by the reference model. In addition, the influence of different flux operators for transporting the potential vorticity (PV) is assessed specifically. It is indicated that the second-order flux operator leads to a spurious increase in the kinetic energy at the tail of the spectrum, whereas the upwind third-order flux operator does not support this behavior owing to implicit numerical diffusion. Moreover, the nonlinear vorticity dynamics is studied by using colliding modons. It is found that the grid-point model maintains the symmetrical pattern of vortices, and generates similar kinetic energy spectra and nonlinear spectral fluxes to the reference model. The evaluation provides a reference for assessing the shallow water model in terms of nonlinear dynamics, and the developed global shallow water model presents a good example.

Key words: kinetic energy spectra, nonlinear vorticity dynamics, shallow water model, icosahedral model, model evaluation

Citation: Wang, L., Y. Zhang, J. Li, et al., 2019: Understanding the performance of an unstructured-mesh global shallow water model on kinetic energy spectra and nonlinear vorticity dynamics. *J. Meteor. Res.*, **33**(6), 1075–1097, doi: 10.1007/s13351-019-9004-2.

1. Introduction

The kinetic energy spectra reflect the essential statistical characteristics of atmospheric motion, showing a k^{-3} power law at large scales and a $k^{-5/3}$ power law at mesoscales between the kinetic energy and wavenumbers (Boer and Shepherd, 1983; Nastrom et al., 1984; Lindborg, 1999). The k^{-3} power law can be explained by the theory of two-dimensional turbulence and quasi-geostrophic turbulence (Charney, 1971; Boer and Shepherd, 1983; Gage and Nastrom, 1986; Lindborg, 1999), whereas the $k^{-5/3}$ power law has two different explanations: upscale kinetic energy cascade based on the theory of two-dimensional turbulence (Lilly, 1983; Falkovich, 1992) and downscale kinetic energy cascade based on the theory of three-dimensional turbulence (Kolmogorov, 1991; Lindborg, 2006). Nonlinear spectral fluxes reflect the energy cascade and can be used to evaluate the performance of models on establishing the transfer of energy between motions at different scale. Since the characteristics of kinetic energy spectra vary little with the latitudes, altitudes, and seasons, it has been treated as a metric to evaluate the performance of the models.

Many studies have been conducted to evaluate numerical models in terms of the statistical characteristics of the atmospheric kinetic energy spectra. Shutts (2005),

Supported by the National Key Research and Development Program of China (2017YFC1502202), National Natural Science Foundation of China (41875135), and Basic Research and Operation Founds of Chinese Academy of Meteorological Sciences (2018Y004).

*Corresponding author: yizhang@cma.gov.cn.

Palmer (2001), and Palmer et al. (2005) evaluated the kinetic energy spectra of the ECMWF global forecast models. Koshyk and Hamilton (2001) found that the high-resolution SKYHI general circulation model from the Geophysical Fluid Dynamics Laboratory (GFDL) can reproduce the characteristics of the kinetic energy spectra for k^{-3} power law at large scales and $k^{-5/3}$ power law at mesoscales. Skamarock (2004) evaluated the kinetic energy spectra of the weather research and Forecasting limited-area model, and analyzed its response to the spin-up time and dissipation.

The kinetic energy spectra are typically decomposed into rotational and divergent components to study the rotational and divergent flow (Koshyk et al., 1999). It is generally believed that the magnitude of the divergent motion in the real atmosphere is much smaller than that of the rotational motion for the large-scale balanced flow (Saujani and Shepherd, 2006). The divergent motion is comparable to, or greater than, the rotational motion in the mesoscale unbalanced motion (Trenberth and Solomon, 1993). The inflection point of the slope of the kinetic energy spectrum is affected by the proportion of the divergent component in the total kinetic energy. For a reasonable model, an accurate simulation of the divergent and rotational components is a basis of simulating the total kinetic energy spectrum and its transition.

The kinetic energy also consists of the stationary and transient components (Koshyk et al., 1999). In the real atmosphere, the stationary flow is generally attributed to topographic and heat forcing, and the transient flow is treated as a result of the baroclinic instability. According to the theory of two-dimensional turbulence, the stationary component dominates large-scale motion and the transient component does smaller scale motion (Boer and Shepherd, 1983). Simulations of the stationary and transient energies are useful metrics to examine whether a model can accurately reproduce the energy cycle of the atmosphere.

The nonlinear vorticity occurs in various types of weather events, such as tornadoes, hurricanes, and extratropical cyclones. The vorticity dynamics is sometimes used to describe the strongly nonlinear motions. Simulation of nonlinear vorticity dynamics is a basic ability of a reasonable model to simulate the weather and climate. Lin et al. (2017) proposed colliding modons to show how two counter-rotating fluid vortices interact with each other in three-dimensional dynamical cores, and how well a model maintains nonlinear vorticity transport. This test can be used to examine the performance of models on nonlinear vorticity dynamics.

Numerical modeling of the atmosphere has made significant progress in recent years with the theoretical development of atmospheric sciences and advances in computer technology. As a major horizontal abstraction of a three-dimensional dry-adiabatic and frictionless atmosphere, the shallow water equations are usually adopted as a prototype for developing a full-fledged general circulation model. A suite of standard test cases proposed by Williamson et al. (1992) is widely used to verify the rationality and stability of shallow water models. These tests are usually used to demonstrate the stability and accuracy of the developed model. To more rigorously assess the performance of a model, the kinetic energy spectra and nonlinear vorticity dynamics also require careful examination. In addition, many earlier studies have discussed the kinetic energy spectra and nonlinear vorticity dynamics of three-dimensional models, whereas seldom studies show them in shallow water environment (e.g., Rípodas et al., 2009).

One purpose of this study is to examine the properties of kinetic energy spectra and nonlinear vorticity dynamics in a shallow-water environment. These performance metrics may be used as a more stringent evaluation for the shallow water model. Meanwhile, the other purpose is to evaluate a newly developed shallow water model on an unstructured mesh. By first providing the characteristics of the kinetic energy spectra and nonlinear vorticity dynamics from the NCAR Spectral Transform Shallow Water Model (STSWM; Hack and Jakob, 1992) as a reference, we then evaluate the unstructured-mesh model against the reference model. Moreover, the effects of the resolution and the potential vorticity (PV) flux operators on the solutions are further explored. All the numerical tests of the unstructured-mesh model are performed using a parallelized model version, which facilitates high-resolution modeling and also has a practical implication for examining the correctness of technical implementation.

The remainder of this paper is organized as follows. Section 2 describes the reference spectral model, the unstructured-mesh shallow water model, the experimental configuration, and analysis methods. Section 3 presents kinetic energy spectra, nonlinear vorticity dynamics of the reference spectral model, and the evaluation of icosahedral model. Section 4 provides the summary and discussion.

2. Model, experiments, and methods

2.1 *NCAR STSWM*

The STSWM is a shallow water model developed by NCAR. It combines a conventional spectral transform technique with a semi-implicit time scheme (Hack and

Jakob, 1992; Jakob-Chien et al., 1995). The resolution of STSWM in this study is truncated at T511 (~25 km). The prognostic variables are absolute vorticity, divergence, and geopotential. For a grid-point model based on the vorticity–divergence momentum equation, the model possesses excellent linear dispersion properties regardless of the resolution (Randall, 1994). While for numerically solving a vorticity–divergence momentum equation, the spectral method is conventionally a more popular choice. The STSWM utilizes computational fourth-order horizontal diffusion terms for all prognostic variables. These numerical viscous-like terms are important in maintaining the solution quality: to provide a way for removing energy accumulated at the truncation limit; otherwise, the model may simulate a kinetic energy spectrum with a problematic high tail due to the spectral blocking problem. Recent study has also suggested that the treatment of the diffusion procedures (low or high order) in the conventional unstaggered A-grid may have a significant impact on the wave propagation (Chen et al., 2018). The horizontal diffusion coefficients are set to 8×10^{12} m^4 s^{-1} for test case 5 and colliding modons, and 5×10^{12} m^4 s^{-1} for test case 6. The Asselin filter coefficient is set to 0.05. The spectral coefficients of the vorticity, divergence, and height are used for analysis.

2.2 *The unstructured-mesh shallow water model*

The construction of the model and related computational algorithms has been described in Zhang (2018). The modeling framework is based on an unstructured Voronoi–Delaunay grid, and can be used for both quasi-uniform and variable-resolution modeling (cf., Zhang et al., 2019). For the quasi-uniform applications studied here, an icosahedron–bisection approach (e.g., Heikes and Randall, 1995) is used to generate grid points on the sphere, and the model is simply referred to as an icosahedral model or a grid-point model. Bisecting each triangular edge of the icosahedron and projecting the points to the sphere leads to one-level finer grids. The resolution after n-round bisection is referred to as grid level n or simply Gn. The Voronoi style hexagonal grid is chosen as the primal cell, and the Delaunay triangular mesh is used as the dual cell. The numbers of the grid points and the equivalent resolution in kilometers for grid level/Gn are listed in Table 1. Moreover, the Spherical Centroidal Voronoi Tessellation (SCVT) technique based on the Lloyd's method (e.g., Ringler et al., 2008; Jacobsen et al., 2013) is used to optimize the grid point location. No explicit diffusion term is used for the grid-point model, but implicit diffusion is supported.

The continuous vector-invariant form shallow water equations may be written as follows:

$$\frac{\partial h}{\partial t} = -\nabla \cdot (h\boldsymbol{V}), \tag{1}$$

$$\frac{\partial \boldsymbol{V}}{\partial t} = -\zeta_p \boldsymbol{k} \times h\boldsymbol{V} - \nabla(\mathrm{g}h + \mathrm{g}b + K), \tag{2}$$

where h is the fluid thickness, $\boldsymbol{V}$ is the horizontal velocity vector, $\zeta_p = \zeta_a/h$ is the shallow-water PV, ζ_a is the absolute vorticity, $\boldsymbol{k}$ is a unit vector along the local vertical direction, b is the topographic height, K is the horizontal kinetic energy, ∇ is the horizontal gradient operator (also referred to as the nabla/del operator), and $\frac{\partial}{\partial t}$ is the local time derivative.

Based on the hexagonal C-grid staggering, three types of geometric locations are constructed as follows (Fig. 1): (1) the mass point is defined at the vertex of the triangle, referred to as primal cell i; (2) the velocity point is defined as the crossing point of a pair of hexagonal and triangular edges, referred to as edge point e; (3) the vorticity point is defined at the circumcenter of the Delaunay triangle, referred to as dual cell v; but note that some alternative definitions are also available in the literature (e.g., Gassmann, 2011). A summary of the major computational procedures and discussions related to the shallow water model are presented in the Appendix of this paper.

2.3 *Experimental configuration*

The pivotal test cases 5 and 6 in Williamson et al. (1992) and colliding modons are conducted for analysis. Test case 5 consists of a zonal flow impinging on an isolated conical mountain located at $\lambda_c = \pi/2$ and $\theta_c = \pi/6$.

Table 1. Numbers of points, edges, triangles, and average interval for grid level/Gn from 3 to 9 with a bisected icosahedron after the SCVT optimization. Note that only grid level/Gn from 4 to 8 is used in this study

Grid level/Gn	Point (N_i)	Edge (N_e)	Triangle (N_t)	Average interval between points (km)
3	642	1920	1280	960.2
4	2562	7680	5120	480.5
5	10,242	30,720	20,480	240.3
6	40,962	122,880	81,920	120.1
7	163,842	491,520	327,680	60.1
8	655,362	1,966,080	1,310,720	30.0
9	2,621,422	7,864,320	5,242,880	15.0

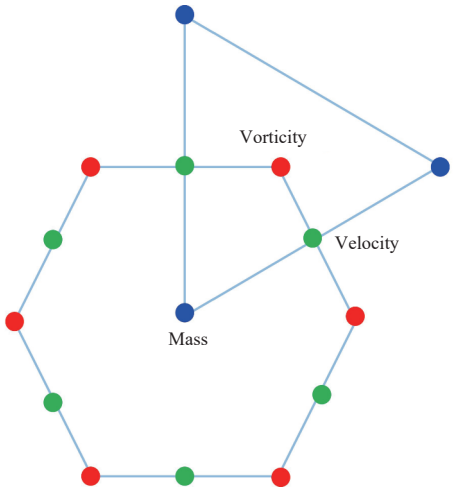

Fig. 1. Hexagonal C-grid staggering of variables in the Voronoi–Delaunay grid. Mass is defined at blue points; velocity is defined at green points; and vorticity is defined at red points.

The height of the mountain is given by:

$$h_s = h_{s0}(1 - r/R), \tag{3}$$

where h_{s0} = 2000 m, $R = \pi/9$, and $r^2 = \min[R^2, (\lambda - \lambda_c)^2 + (\theta - \theta_c)^2]$. Test case 6 consists of a large-scale rotating fluid, and the detailed descriptions about the test case 6 can be found in Williamson et al. (1992). The initial state is a Rossby–Haurwitz wave of wavenumber 4 as suggested by Hoskins (1973). The examination of results follows the standard practice (two weeks) of Jakob–Chien et al. (1995), while a longer duration is supported (e.g., 30 days). The tests are run at the resolution of G4–G8 to evaluate the performance of the icosahedral model at multiple resolutions.

The test case of colliding modons is designed to test whether a dynamic core can maintain the symmetrical pattern of the modons (Lin et al., 2017). This test is proposed to compensate for the weakness of the Rossby–Haurwitz wave test, which is not stable over long duration due to weak perturbations and mesh irregularity (Thuburn and Li, 2000). The colliding modons test is not affected by the initial field and is stable. The modon is defined by the zonal wind perturbation:

$$M_i = U_0 e^{\left[-(r_i/r_0)^2\right]}, \tag{4}$$

where U_0 = 40 m s^{-1}, r_0 = 500 km, and r_1 and r_2 are the great circle distances from the center of each modon. The modons are initially located at $(\pi/2, 0)$ and $(3\pi/2, 0)$. The two initial opposite zonal wind perturbations are given by:

$$u'(\lambda, \theta) = M_1 - M_2, \tag{5}$$

where λ and θ are longitude and latitude, respectively. The test for the icosahedral model is performed at the resolution of G7 and integrated for 100 days to analyze the propagation of the modons.

2.4 *Analysis methods*

The kinetic energy spectrum represents the relationship between the kinetic energy and wavenumbers. It is calculated using vorticity and divergence in this study. The spectral coefficients of the vorticity and divergence are obtained by spherical harmonic expansion first, then the kinetic energy spectrum is calculated as in Jakob-Chien et al. (1995):

$$\mathrm{KE}_n = \frac{a^2}{4n(n+1)}\left[\zeta_n^0\left(\zeta_n^0\right)^* + \delta_n^0\left(\delta_n^0\right)^* + 2\sum_{m=1}^{n}\zeta_n^m(\zeta_n^m)^* + 2\sum_{m=1}^{n}\delta_n^m(\delta_n^m)^*\right], \tag{6}$$

where a is the radius of the earth, n is the total wavenumber, ζ_n^m is the spectral coefficient of the vorticity, δ_n^m is the spectral coefficient of the divergence, m is the zonal wavenumber, and $()^*$ represents the complex conjugate.

The rotational and divergent kinetic energy spectra are calculated by only using the spectral coefficient of vorticity and divergence, respectively. They follow the Eqs. (7) and (8):

$$\mathrm{KE}_n^{\mathrm{rot}} = \frac{a^2}{4n(n+1)}\left[\zeta_n^0\left(\zeta_n^0\right)^* + 2\sum_{m=1}^{n}\zeta_n^m(\zeta_n^m)^*\right], \tag{7}$$

$$\mathrm{KE}_n^{\mathrm{div}} = \frac{a^2}{4n(n+1)}\left[\delta_n^0\left(\delta_n^0\right)^* + 2\sum_{m=1}^{n}\delta_n^m(\delta_n^m)^*\right]. \tag{8}$$

The stationary and transient kinetic energy spectra are calculated by using Eqs. (9) and (10) (Koshyk et al., 1999), respectively.

$$\mathrm{KE}_n^{\mathrm{sta}} = \frac{a^2}{4n(n+1)}\sum_{m=-n}^{n}\left(\left|\overline{\zeta_n^m}\right|^2 + \left|\overline{\delta_n^m}\right|^2\right), \tag{9}$$

$$\mathrm{KE}_n^{\mathrm{tra}} = \frac{a^2}{4n(n+1)}\sum_{m=-n}^{n}\left(\overline{\left|\zeta_n^{m'}\right|^2} + \overline{\left|\delta_n^{m'}\right|^2}\right), \tag{10}$$

where the overbar denotes the time mean, and the prime denotes the deviation from the mean.

The kinetic energy spectra of the STSWM is calculated directly using the spectral coefficients. For the grid-point model that does not have spectral coefficients, the divergence and vorticity are first interpolated to the Gaussian grid with 40, 80, 160, 320, and 640 latitudinal grid points for the G4–G8 tests (ensuring that the horizontal intervals are close to each other before and after the interpolation). The Inverse Distance Weighted Interpolation method is applied here, which reads

$$z_g = \frac{\sum_{i=1}^{n}\left(\frac{z_i}{D_i^2}\right)}{\sum_{i=1}^{n}\left(\frac{1}{D_i^2}\right)}, \tag{11}$$

$$D_i = \sqrt{\left(x_g - x_i\right)^2 + \left(y_g - y_i\right)^2}, \tag{12}$$

where z_g is the estimated value, z_i is the value on original grid, $\left(x_g, y_g\right)$ and (x_i, y_i) are the horizonal position of the estimated grid and the original grid, and D_i is the distance between them. The spectral coefficients of the divergence and vorticity from the scalar spherical harmonic transforming process are then used to calculate the kinetic energy spectra of the icosahedral model.

The nonlinear spectral fluxes are calculated to examine the energy cascade: the energy transfers from large to small scale or vice versa at a fixed wavelength. The nonlinear interaction of rotational flow conserves kinetic energy and enstrophy. The enstrophy spectrum can be calculate by:

$$G_n = \frac{n(n+1)}{a^2}\mathrm{KE}_n^{\mathrm{rot}}. \tag{13}$$

The kinetic energy and enstrophy fluxes are calculated following Burgess et al. (2013). The interaction terms should be calculated first, which means that the flow at wavenumber n gains or loses energy. The enstrophy interaction term is calculated by:

$$J_n = -\frac{1}{4}\sum_{m=-n}^{n}\left[\zeta_n^{m*}(\boldsymbol{v}\cdot\nabla\zeta)_n^m + \zeta_n^m(\boldsymbol{v}\cdot\nabla\zeta)_n^{m*}\right], \tag{14}$$

where ζ is the vorticity, $\boldsymbol{v}$ is the rotational velocity vector, $()_n^m$ represents the spectral coefficient, and $()_n^{m*}$ represents the complex conjugate. In this equation, ζ and $\boldsymbol{v}\cdot\nabla\zeta$ should be calculated at each grid for each day, and then decomposed into spherical harmonics. The kinetic energy interaction term is calculated by:

$$I_n = \frac{a^2}{n(n+1)}J_n, \tag{15}$$

where a is the earth radius and n is the total wavenumber.

As the physical meaning of the nonlinear spectral fluxes, the enstrophy and kinetic energy flux should be sum of all the interaction terms of wavenumbers less than the fixed wavenumber n. The enstrophy flux of wavenumber $n + 1$ is given by:

$$H_{n+1} = -\sum_{l=0}^{n} J_l, \tag{16}$$

and the kinetic energy flux of wavenumber $n + 1$ is presented by:

$$F_{n+1} = -\sum_{l=0}^{n} I_l. \tag{17}$$

3. Results

This section discusses the kinetic energy spectra and nonlinear spectral fluxes of the shallow water model in three test cases and examines the characteristics of nonlinear vorticity transport using colliding modons. The results from the STSWM are firstly shown and the grid-point model is then evaluated.

3.1 *Zonal flow over an isolated mountain*

The predicted variables, height and velocity of zonal flow in the test case 5 after 16 days derived from the STSWM and the icosahedral model at the resolution of G4–G8, are firstly shown in Fig. 2. There is a good agreement in the height fields between the grid-point model and STSWM solutions when the resolution is enhanced to G6. The difference in the velocity field between the two models decreases with the improvement of resolution, and the improvement of velocity simulation is especially evident when the resolution improved from G4 to G6.

Figure 3 shows the kinetic energy spectra of the numerical simulations from the STSWM and the icosahedral model at the resolution of G4–G8. The kinetic energy spectrum of the STSWM has two inflection points at wavenumbers 2 and 7. The kinetic energy decreases from wavenumbers 1 to 2, increases until wavenumber 7, then drops off with the increase of wavenumbers, which means that the large scale motion is mainly contributed by wavenumbers 1 and 7. The kinetic energy spectra of the grid-point model are in good agreement with the spectra of the STSWM. At higher model resolutions, the smaller wavelength of the spectrum lies closer to that of the STSWM. The kinetic energy spectrum of the icosahedral model extends to smaller scales as the resolution increases.

To evaluate the effect of various PV transport schemes (see Appendix) on the kinetic energy spectra at the resolution of G5–G8, the second- and third-order flux operators for PV transport (PV2 and PV3, respectively) are evaluated. Figure 4 shows the averaged kinetic energy spectra of the icosahedral model with two different flux operators. The kinetic energy in the PV2 run is larger than that in the PV3 run at the tail of the spectrum; the difference is smallest at G8, implying that high resolution is helpful to reduce the errors associated with the PV schemes. The differences in the kinetic energy between the PV2 and PV3 tests are a result of the fact that no implicit diffusion is supported by PV2, which precludes the transfer of potential enstrophy to the sub-grid scale. PV3 has an implicit diffusion term (see Appendix), which

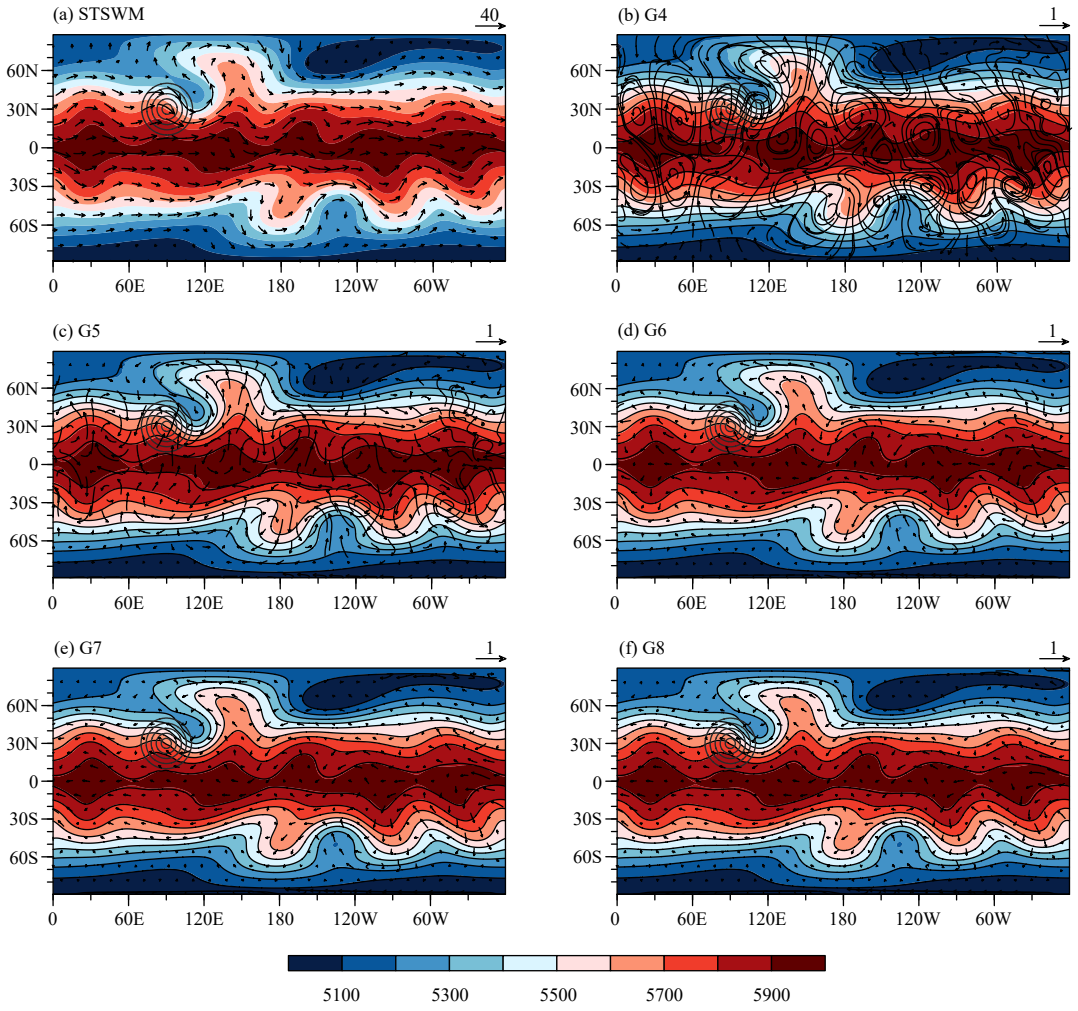

Fig. 2. (a) The NCAR STSWM T511 (STSWM) height (shading; m) and velocity (vectors; m s^{-1}) fields after 16 simulation days; (b–f) the icosahedral-model height fields (shading; m), the STSWM reference height fields (black contour lines), and the difference of velocity fields (vectors; m s^{-1}) between the icosahedral model and the STSWM after 16 days. The icosahedral model is configured at (b–f) G4–G8, respectively. The reference vector (m s^{-1}) of velocity is indicated on the top right of each panel.

helps to remove grid-scale oscillations and smooth the short wavelength signal. The lack of a diffusion procedure leads to a spurious increase in energy at small scales. The remaining discussion of the icosahedral model is based on the results using PV3.

Figure 5 demonstrates the total kinetic energy spectra, and the rotational and divergent components from the STSWM and the icosahedral model at the resolution of G4–G8. As shown in Fig. 5a, the rotational kinetic energy contributes to most of the total kinetic energy, and is much larger than the divergent kinetic energy at large scales (wavenumbers less than 80). The divergent component fluctuates with an amplitude of about one order of magnitude at wavenumbers 10–80, and is almost equivalent to the rotational component at wavenumbers larger than 80. At the scale of wavenumbers larger than 200, the rotational component reduces rapidly with the wavenumber, and the divergent component dominates the total kinetic energy. The rotational components simulated by the icosahedral model at five resolutions (Figs. 5b–f) are consistent with the solutions of the STSWM. Nevertheless, the rotational components are still slightly larger than the divergent components at wavenumbers larger than 200 in two high-resolution tests (G7 and G8). The icosahedral model simulates the fluctuation of the divergent component, but the divergent kinetic energy does not show evident reduction in the spectrum tail as compared to the STSWM, probably due to the different diffusion strength of the two models.

As the rotational component dominates the total kinetic energy at large scales, more emphasis is laid on this component. The nonlinear flux represents the spectral transfer of energy due to nonlinear interactions, in which a negative flux represents an upscale transmission and a

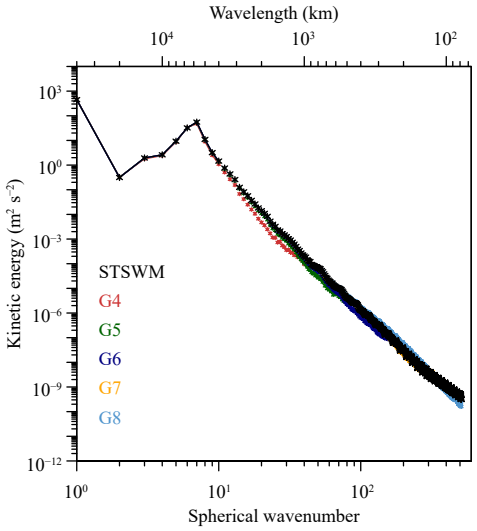

Fig. 3. Kinetic energy spectra averaged from Days 5 to 16 in the test case 5 from the NCAR STSWM T511 (STSWM; ~25 km) and the icosahedral model configured at G4 (~480 km)–G8 (~30 km).

positive flux represents a downscale transmission. Figure 6a shows that there is an evident upscale transmission of kinetic energy flux at wavenumbers 5, 6, and 7 and a downscale transmission of kinetic energy flux when the wavenumber is 4 or greater than 8. This means that wavenumber 4 gains kinetic energy and wavenumber 7 loses kinetic energy. A slight upscale transmission of kinetic energy exists at wavenumber 3, indicating that wavenumber 2 gains kinetic energy from smaller scales. The kinetic energy budget of wavenumbers 2 and 7 is consistent with the inflection of these wavenumbers seen in Fig. 3. The downscale kinetic energy fluxes are less than one-half of the upscale kinetic energy fluxes. The enstrophy flux is 12 orders of magnitude smaller than the kinetic energy flux (Fig. 6b). The signs of the enstrophy flux are same as those of the kinetic energy flux, and the downscale fluxes are roughly the same magnitude as the upscale fluxes. Compared with the STSWM, the icosahedral model generates consistent solutions from G5 to

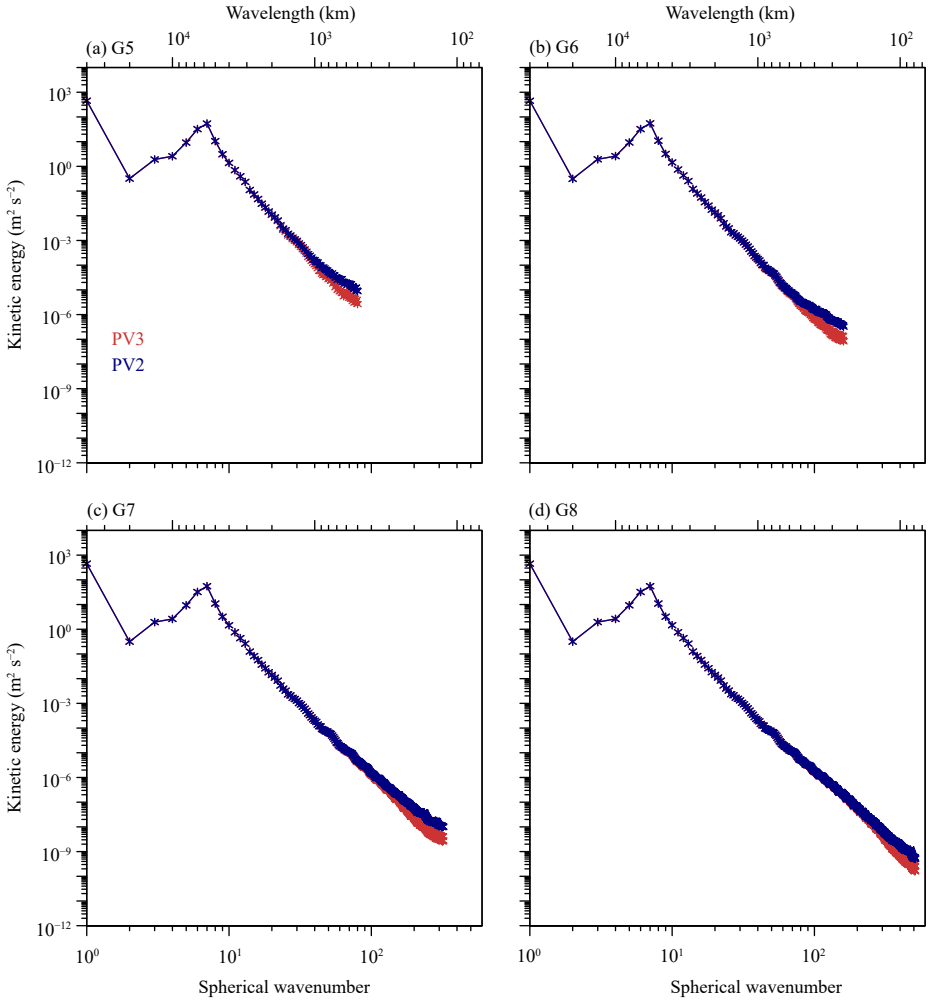

Fig. 4. Kinetic energy spectra of the icosahedral model with the second-order (PV2; blue color) and the third-order (PV3; red color) flux operators averaged from Days 5 to 16 in the test case 5. The icosahedral model is configured at (a) G5, (b) G6, (c) G7, and (d) G8, respectively.

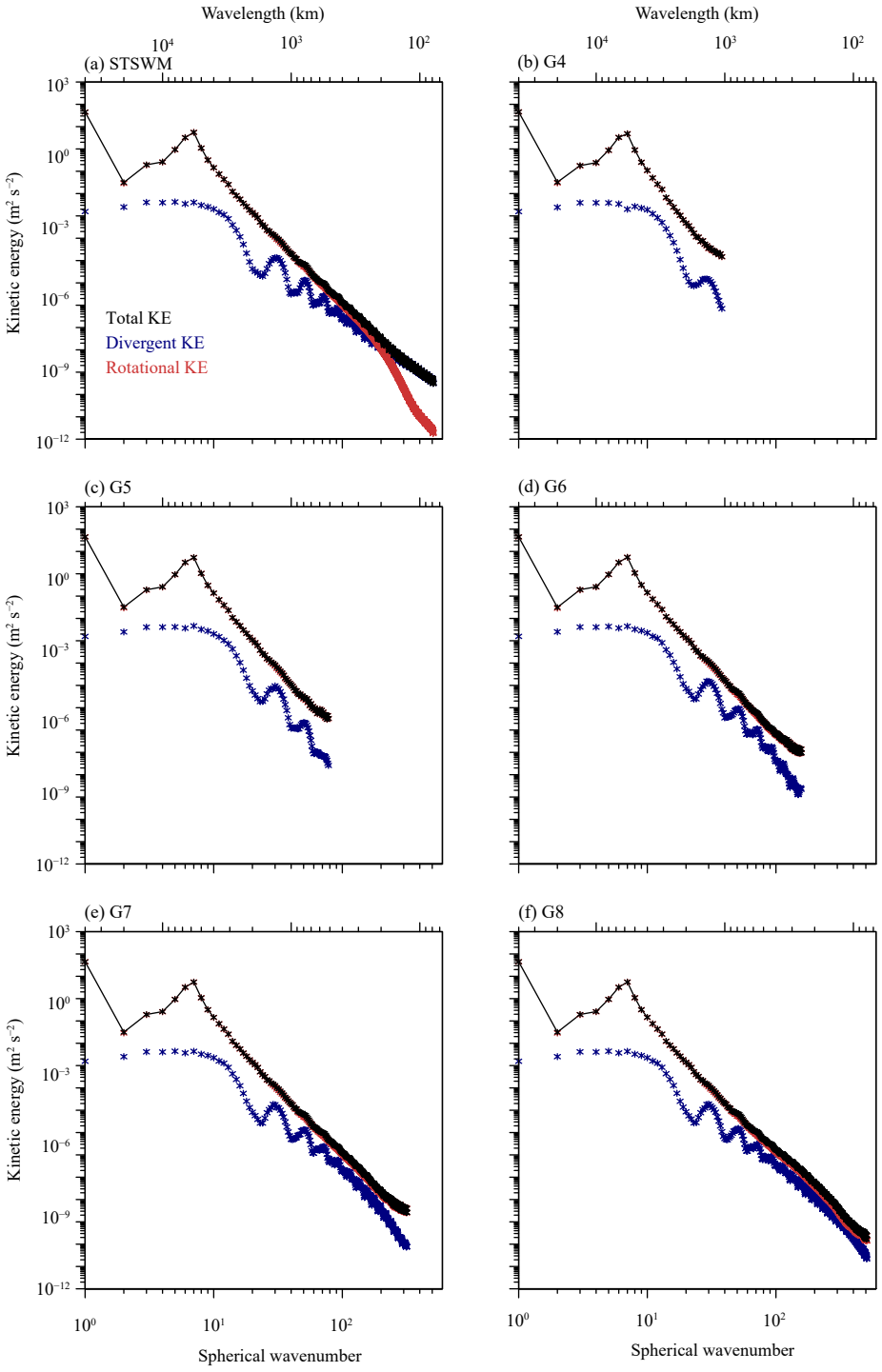

Fig. 5. Total kinetic energy (KE) spectra (black color), and the rotational (red color) and divergent (blue color) components averaged from Days 5 to 16 in the test case 5 from (a) the STSWM and (b–f) the icosahedral model configured at G4–G8, respectively.

G8. The G4 resolution is too coarse to produce a reasonable result as the reference model does.

To evaluate the contribution of stationary and transient flows to atmospheric motion at various scales in the shallow water model, the total kinetic energy is further decomposed into stationary and transient components (Fig. 7). Figure 7a exhibits the results obtained from the STSWM. The total kinetic energy spectrum at wavenumbers smaller than 8 is largely contributed by the stationary component, except for wavenumber 3. The transient kinetic energy is higher than the stationary component until wavenumber 150, then drops off rapidly with in-

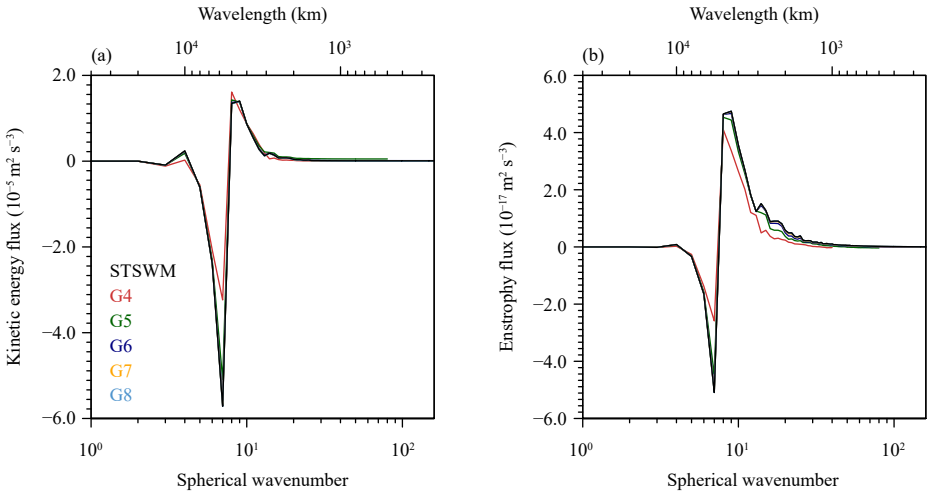

Fig. 6. (a) Rotational kinetic energy fluxes and (b) enstrophy fluxes on Day 15 in the test case 5 from the STSWM and the icosahedral model configured at G4–G8.

creases in the wavenumber at the tail of the spectrum. Figures 7b–f show that the solutions of the icosahedral model at multiple resolutions have similar characteristics in that the stationary component dominates the total kinetic energy at large scales. The transient component dominates at smaller scales, but again becomes smaller than the stationary kinetic energy at the spectrum tail. With an increase of resolution, the dominance of the transient component is able to extend to smaller scales. Nevertheless, the transient energy at the spectral tail at G7 and G8 is still larger than that in the reference model.

3.2 *Rossby–Haurwitz wave*

This section examines the solutions of the Rossby–Haurwitz wave in test case 6 from the STSWM and the icosahedral model. The height and velocity fields of a Rossby–Haurwitz wave of wavenumber 4 after 14 days derived from the STSWM and the icosahedral model at the resolution of G4–G8 are shown in Fig. 8. The height fields simulated by the icosahedral model are highly consistent with that of the STSWM after the mesh refinement to G6. The differences of the velocity between the icosahedral model simulation and the reference solution decrease from more than 10 m s^{-1} at G4 to less than 1 m s^{-1} at G8. Together with Fig. 2, results demonstrate that the numerical errors at G6 (~100 km) is small enough as compared to the reference model, suggesting that G6 might be the choice of the coarsest operational resolution for practical modeling.

Figure 9 shows that the kinetic spectrum of the Rossby–Haurwitz wave test from the STSWM and the icosahedral model at the resolution of G4–G8 forms two branches because the kinetic energy at odd wavenumbers is several orders of magnitude higher than that at even wavenumbers. Since the initial field should ideally have zero divergence, the kinetic energy is mainly contributed by the rotational motion. The odd wavenumber kinetic energy spectrum of the STSWM shows a k^{-3} dependence in the wavenumber range 20–160, which seems to preserve certain characteristics of the kinetic energy spectra of the motion in the real atmosphere. The decrease at wavenumbers larger than 160 may be related to numerical diffusion. The kinetic energy at odd wavenumbers simulated by the icosahedral model is consistent with that simulated by the STSWM, and the spectra extend to smaller scales as the resolution increases. The odd wavenumber kinetic energy at G7 is closest to the STSWM. At the highest resolution (G8), the results of the icosahedral model are even closer to the k^{-3} slope than the spectral model, indicating that the icosahedral model may have certain superiority if we compare results against the reference slope line. The kinetic energy at even wavenumbers simulated by the icosahedral model is larger than that simulated by the STSWM when the wavenumber is larger than 15, suggesting that more divergence is generated. With an increase in the resolution, the kinetic energy at even wavenumbers becomes smaller at the spectrum tail, closer to that in the reference model. This reflects the fact that more small-scale motions are resolved reasonably by high-resolution modeling.

Figure 10 displays the influence of PV2 and PV3 on the simulated kinetic spectra from the icosahedral model at the resolution of G4–G8. As a result of the lack of implicit diffusion in PV2, the kinetic energy at the spectrum tail in the PV2 run is larger than that in the PV3 run. This can be more clearly observed at odd wavenumbers than at even wavenumbers, indicating that the implicit diffusion in PV3 mainly affects the rotational motion.

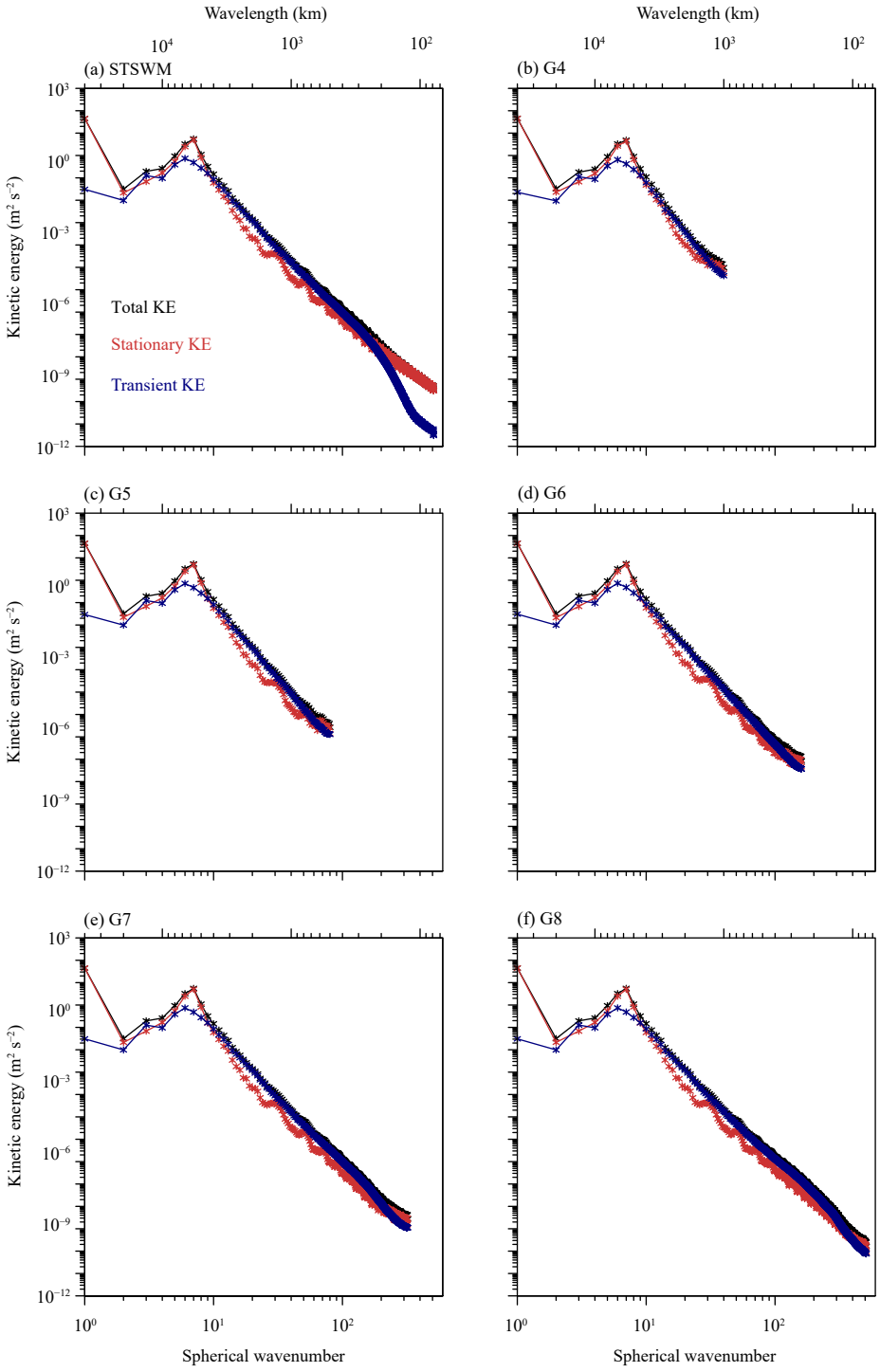

Fig. 7. Total kinetic energy (KE) spectra (black color), and the stationary (red color) and transient (blue color) components averaged from Days 5 to 16 in the test case 5 from (a) the STSWM and (b–f) the icosahedral model configured at G4–G8, respectively.

The starting point for the spurious increase in kinetic energy spectra in the PV2 run moves toward smaller scales as the resolution increases, that is, the implicit diffusion in PV3 mainly affects the smallest resolvable scale. The following discussion focuses on the results from the PV3 tests.

We decompose the total kinetic energy into divergent and rotational components. Figure 11 shows that, for the STSWM, the rotational component contributes to the odd wavenumber energy, whereas the divergent component contributes to the even wavenumber energy, further explaining the two branches in Fig. 9. In the simulation of

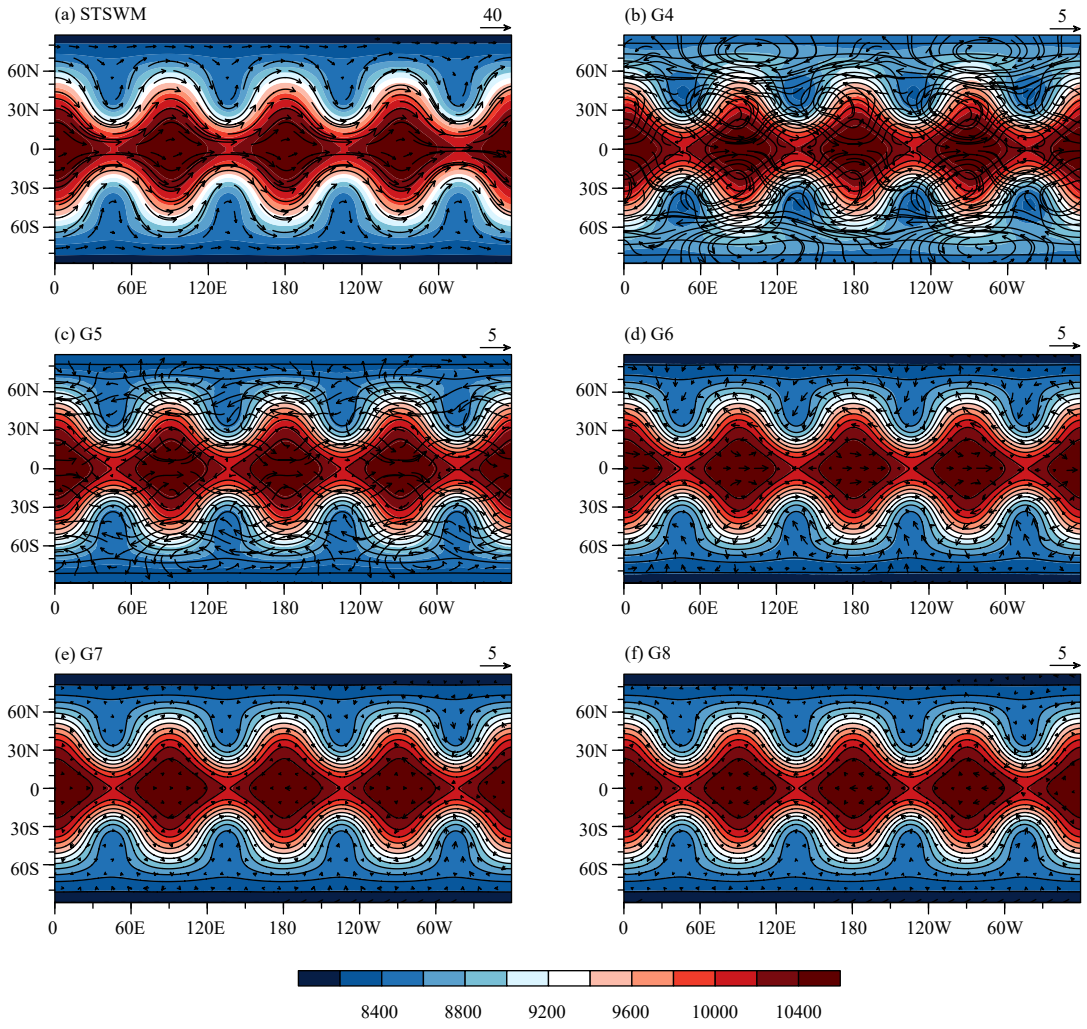

Fig. 8. As in Fig. 2, but for the test case 6 after 14 days.

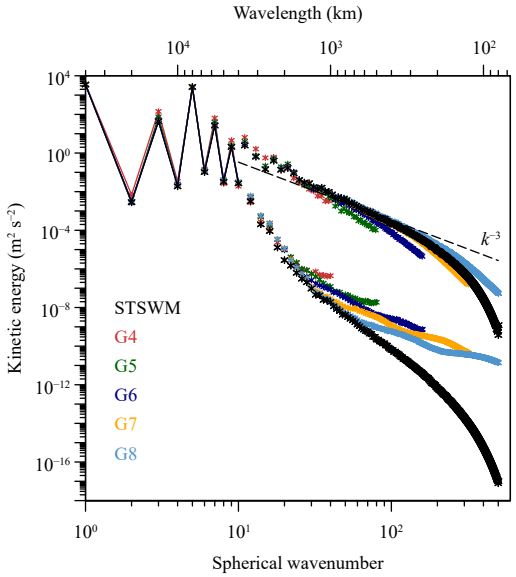

Fig. 9. Kinetic energy spectra averaged from Days 5 to 14 in the test case 6 from the STSWM and the icosahedral model configured at G4–G8.

the grid-point model, the rotational component dominates the odd wavenumber kinetic energy, and the divergent component dominates the even wavenumber kinetic energy, consistent with the reference model.

Figure 12 shows the kinetic energy and enstrophy fluxes from the STSWM and the icosahedral model at the resolution of G4–G8 for investigating the spectral transfer of energy. A downscale kinetic energy flux is found at wavenumbers 4 and 5, whereas an upscale kinetic energy flux is found at wavenumbers 6 and 7, indicating that wavenumbers less than 7 overall gain kinetic energy from the smaller scales. The magnitude of the upscale enstrophy fluxes (Fig. 12b) nearly doubles that of the downscale fluxes, and the signs of the fluxes are consistent with those of the kinetic energy fluxes. The icosahedral model simulates the characteristics of the nonlinear spectral fluxes, except that the G4 resolution is very coarse and leads to an upscale transfer of kinetic energy at wavenumbers 2 and 3, which is not observed in the

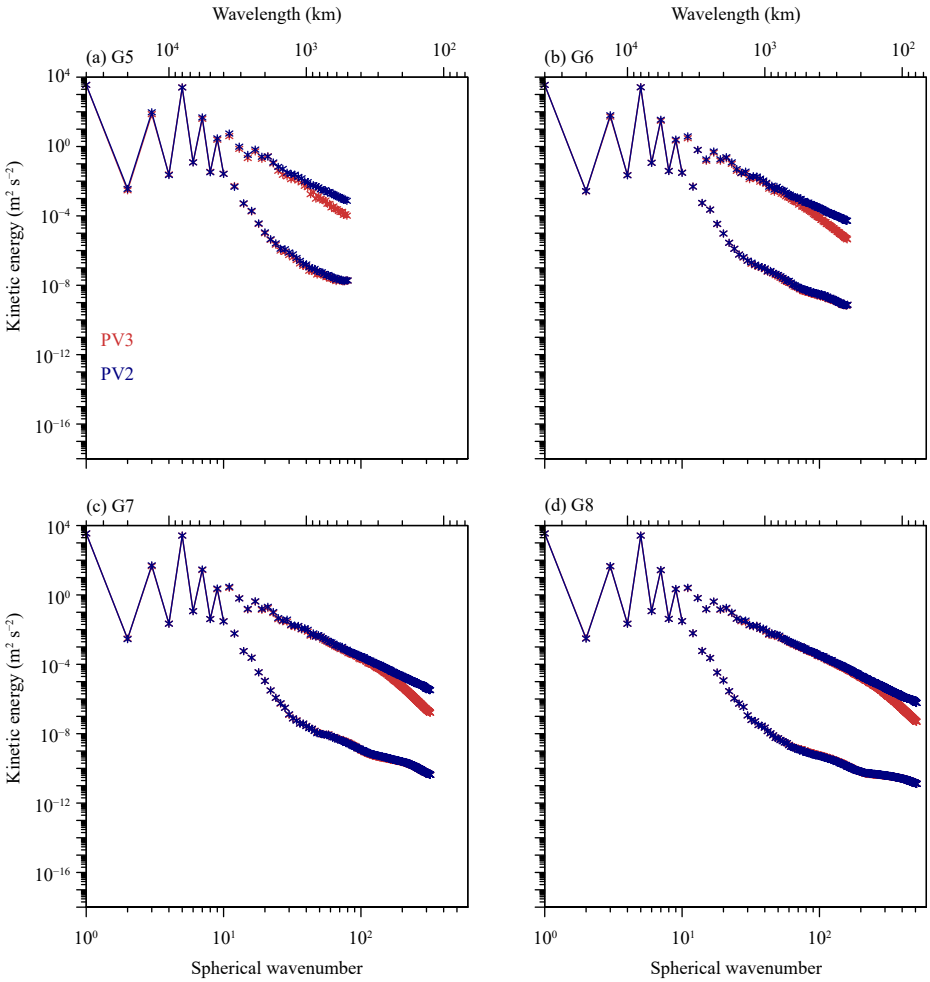

Fig. 10. Kinetic energy spectra of the icosahedral model with the second-order (PV2; blue color) and third-order (PV3; red color) flux operators averaged from Days 5 to 14 in the test case 6. The icosahedral model is configured at (a) G5, (b) G6, (c) G7, and (d) G8, respectively.

reference model. The spectral fluxes approach the reference simulations as the resolution increases.

Figure 13 presents the total kinetic energy, and the stationary and transient components from the STSWM and the icosahedral model at the resolution of G4–G8. The stationary kinetic energy dominates the total kinetic energy at wavenumbers 1, 3, and 7, whereas the transient kinetic energy contributes most of the total kinetic energy at other wavenumbers. The stationary and transient kinetic energies of the odd wavenumbers are larger than those of the even wavenumbers. The kinetic energy spectra simulated by the icosahedral model exhibit comparable characteristics to the reference model, and the increase of resolution helps to improve the performance of this metric.

3.3 *Colliding modons*

The nonlinear vorticity dynamics of the shallow water model is evaluated by using colliding modons. Figure 14 shows the vorticity values simulated by three models: the STSWM and the icosahedral model with PV2 and PV3 at the resolution of G7. Consistent with Lin et al. (2017), the results of STSWM show that modons start to propagate toward each other along the equator on Day 1, then collide and exchange vortices between Days 20 and 30. After colliding, the new modon pairs propagate toward the poles, reaching the poles between Days 40 and 50. They travel across the poles and return to the equator, then collide and exchange vortices for the second time, and form new modon pairs around Day 70. The new modon pairs propagate back to the initial position between Days 90 and 100 and begin a new cycle. The icosahedral model maintains the original modon pair in both the PV2 and PV3 runs. Note that for this case, the PV3 run is combined with $\mathrm{NCT}_{\mathrm{local}}$ while the PV2 run is combined with $\mathrm{NCT}_{\mathrm{non\_local}}$ (see Appendix), to be consistent with the choice in a 3D model. The PV3 test slows the propagation speed of the modon pairs, and they

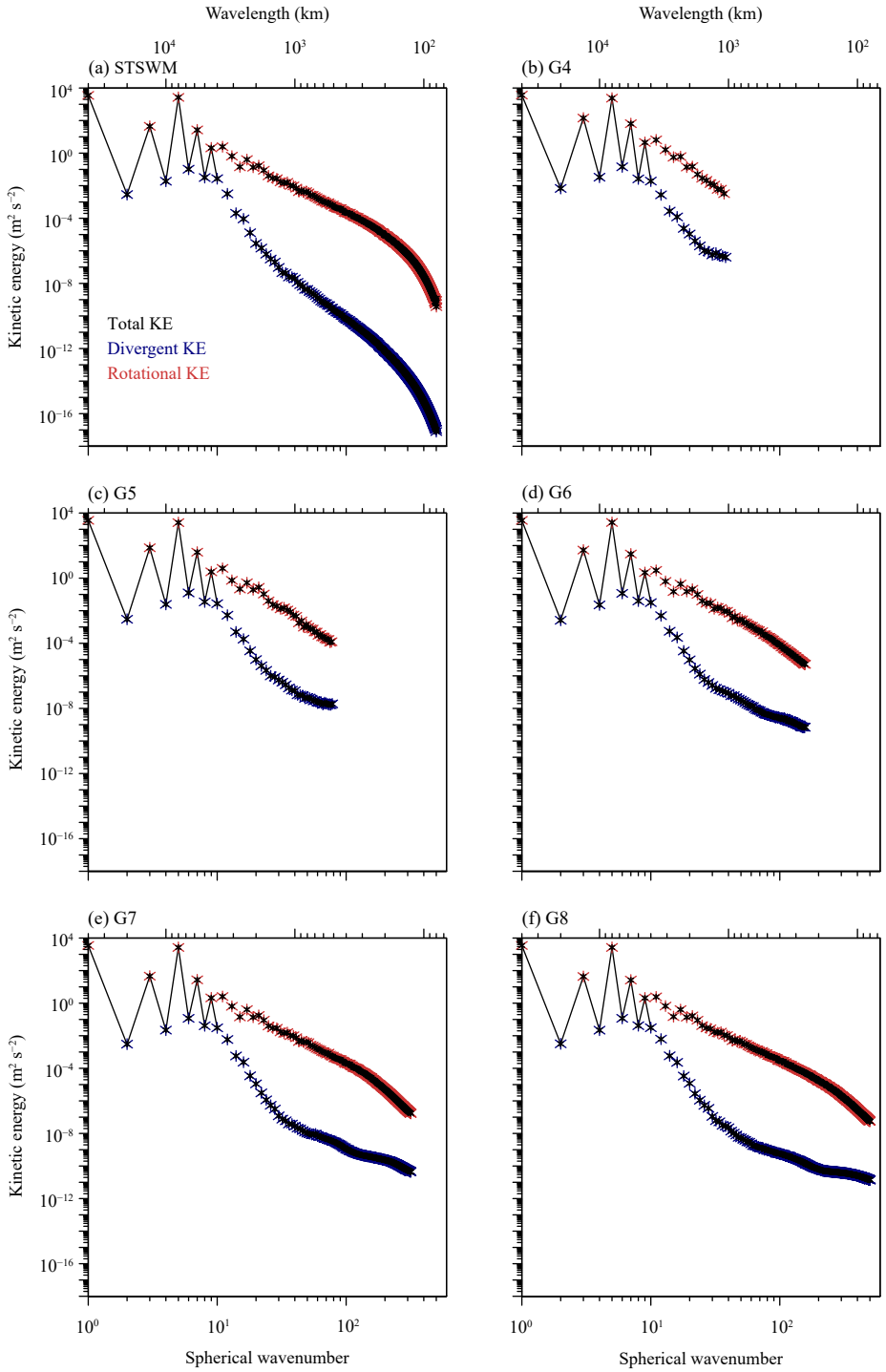

Fig. 11. Total kinetic energy (KE) spectra (black color), and the rotational (red color) and divergent (blue color) components averaged from Days 5 to 14 in the test case 6 from (a) the STSWM and (b–f) the icosahedral model configured at G4–G8, respectively.

return to their initial location on Day 100, five days slower than in the reference model. As studied in Zhang et al. (2019), this slower phase is actually due to the choice of the NCT term, rather than the PV flux operator. For more details regarding the behaviors of modons in a 3D model, see Zhang et al. (2019).

Figure 15 shows the time series of the domain maximum and minimum vorticity values and helps to evaluate the simulation of the amplitude. The amplitude of the modon simulated by the STSWM decays with time, and the maximum and minimum vorticities appear in pairs, with the absolute values roughly equal on the same day. The amplitude of the modon decays in the PV3 run, whereas it appears to develop over time in the PV2 run. The vor-

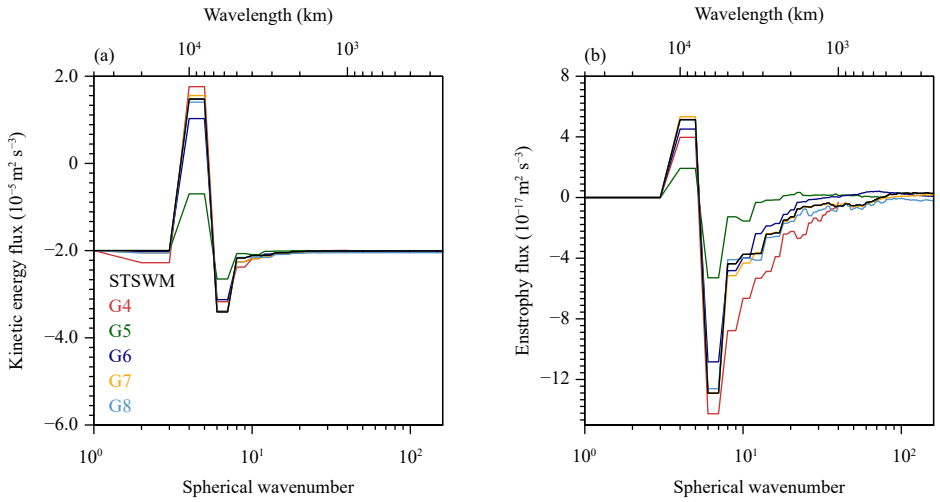

Fig. 12. (a) Rotational kinetic energy fluxes and (b) enstrophy fluxes on Day 12 in the test case 6 from the STSWM and the icosahedral model configured at G4–G8.

tex simulated by PV3 becomes weaker than that in the STSWM from Day 47. The increase in the amplitude in the PV2 run is expected because PV2 has no implicit diffusion. In addition, the vorticity oscillation over time in the icosahedral model is slightly more evident than that in the reference model. This is probably because that the spectral model directly prognoses vorticity and adds an explicit horizontal diffusion term to the vorticity, so the vorticity magnitude may be more steadily maintained.

The kinetic energy spectra of the colliding modons are shown to further evaluate the simulation of nonlinear vorticity dynamics. Figure 16 shows the kinetic energy spectra of the STSWM and the icosahedral model at G7 using PV2 and PV3. As shown in STSWM, the kinetic energy increases with total wavenumbers less than 20 (close to the wavelength of the vortex motion) and decays at wavenumbers larger than 20. The grid-point model simulates the same characteristics of the total kinetic energy as the reference model, but the values are larger. The kinetic energy spectra using PV2 are larger at the spectral tail than those using PV3. Both PV3 and PV2 runs show more oscillated solutions than the reference model, consistent with the results in Fig. 15.

Figure 17 gives the nonlinear spectral fluxes of the kinetic energy and enstrophy on Day 71 for PV2 and the STSWM and on Day 74 for PV3, considering that the modons in the PV3 run propagate slightly slower. There is an upscale transition of the kinetic energy at wavenumbers less than 21 and between 35 and 44, and a downscale transition at wavenumbers between 21 and 35 (Fig. 17a). The icosahedral model generates more kinetic energy fluxes than the reference model. The enstrophy fluxes (Fig. 17b) are at least 10 orders of magnitude smaller than the kinetic energy fluxes. The largest upscale transition of the enstrophy fluxes is in the wavenumber range 19–33 and is nearly double the largest downscale enstrophy fluxes in the wavenumber range 33–44. The PV3 test more consistently simulates the enstrophy fluxes as the reference model, whereas the PV2 test simulates slightly larger enstrophy fluxes. The nonlinear interaction is vigorous at wavenumbers less than 60.

4. Summary and discussion

4.1 *Summary*

We have discussed the kinetic energy spectra and nonlinear vorticity dynamics of a shallow water model STSWM as a benchmark solution, and evaluated the performance of a newly developed shallow water model on an unstructured icosahedral grid using idealized experiments. Our conclusions can be summarized as follows.

In the mountain test, the rotational and divergent kinetic energy dominates the total kinetic energy at large and small scales, respectively. An upscale transition of the kinetic energy and enstrophy fluxes is present at small wavenumbers and a downscale transition appears at larger wavenumbers. The stationary and transient component contributes most of the total kinetic energy at small and large wavenumbers, respectively.

In the Rossby–Haurwitz wave test, the kinetic energy spectrum forms two branches with the kinetic energy at odd wavenumbers larger than that at even wavenumbers. The rotational kinetic energy contributes to most of the odd wavenumber kinetic energy in the Rossby–Haurwitz wave test, and the divergent component dominates the

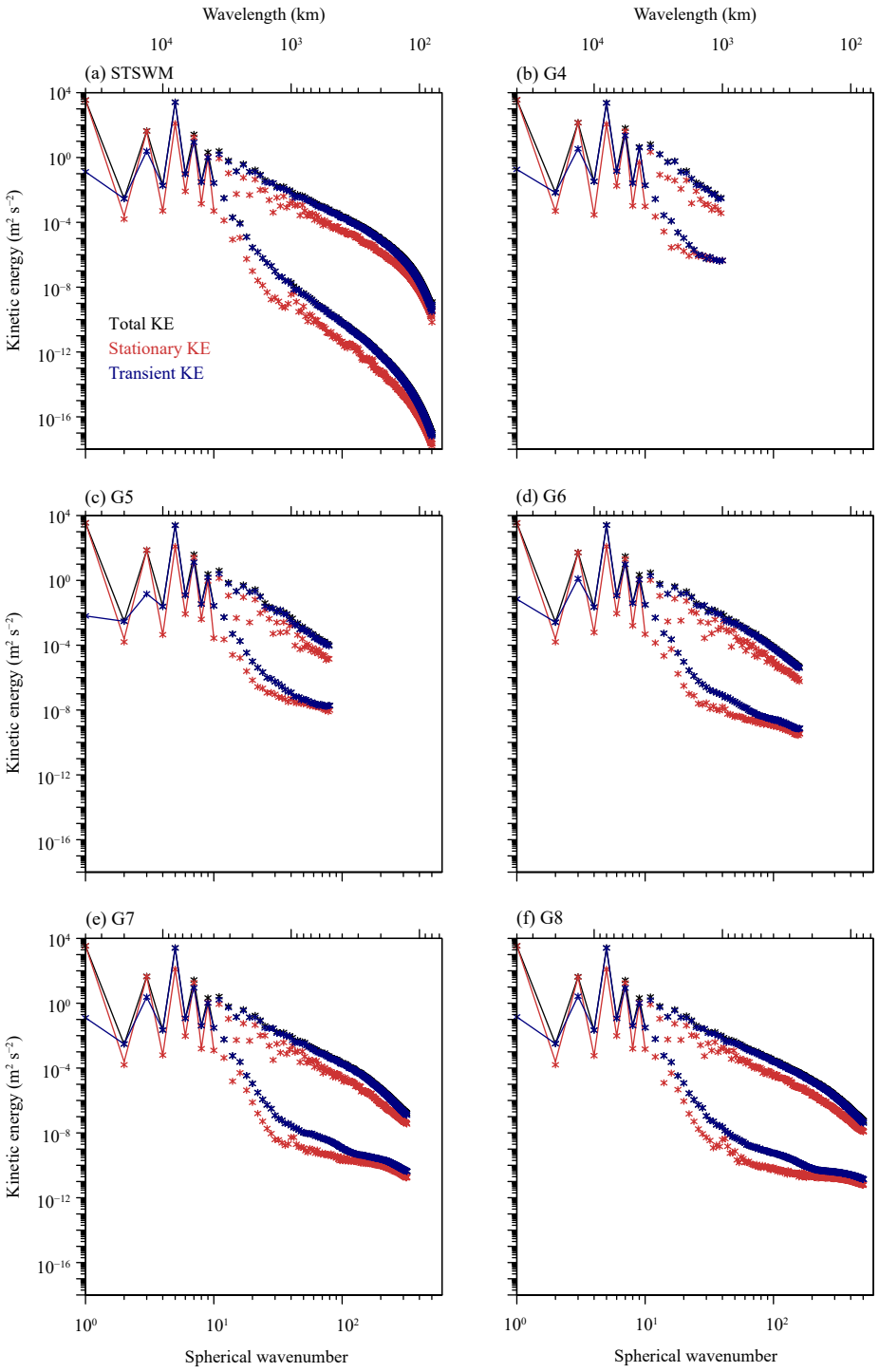

Fig. 13. Total kinetic energy (KE) spectra (black color), and the stationary (red color) and transient (blue color) components averaged from Days 5 to 14 in the test case 6 from (a) the STSWM and (b–f) the icosahedral model configured at G4–G8, respectively.

even wavenumber kinetic energy. A downscale transition of the kinetic energy and enstrophy flux appears at small wavenumbers, and an upscale transition appears at larger wavenumbers. The transient component dominates the total kinetic energy at most wavenumbers except for wavenumbers 1, 3, and 7.

The colliding modons test shows that, in a shallow water model, the vortex pairs propagate along the equator, collide and propagate across poles, collide again and propagate back to the initial position in 100 days. The amplitude of vortex decays over time, and the maximum and minimum vorticity appear in pairs. The kinetic en-

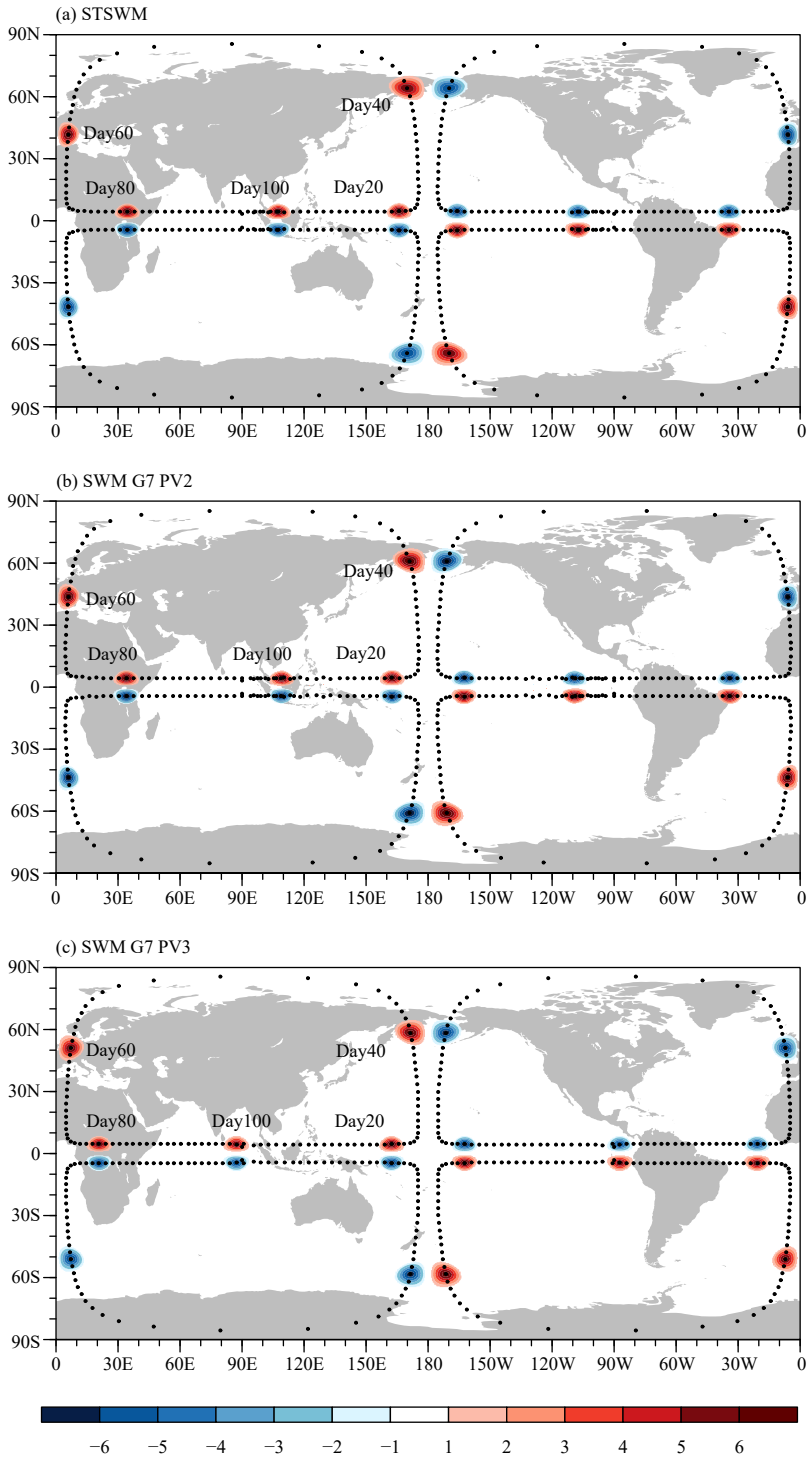

Fig. 14. Relative vorticity (shading) on Days 20, 40, 60, 80, and 100 and the trajectories of the vortices (denoted by black dots) in the test case of colliding modons from (a) the STSWM and the icosahedral model with (b) PV2 and (c) PV3 configured at G7.

ergy spectrum indicates that a slight increase occurs at wavenumbers less than 20, and then the energy decreases as the total wavenumber increases. The nonlinear spectral fluxes, including the kinetic energy and enstrophy fluxes, fluctuate between wavenumbers 3 and 60, suggesting that there are both upscale and downscale energy transitions in motion within these scales.

The features of kinetic energy spectra, the rotational and divergent components, the stationary and transient components, and the spectral fluxes simulated by the icosahedral model and examined in the mountain test and the Rossby–Haurwitz wave test agree well with those in

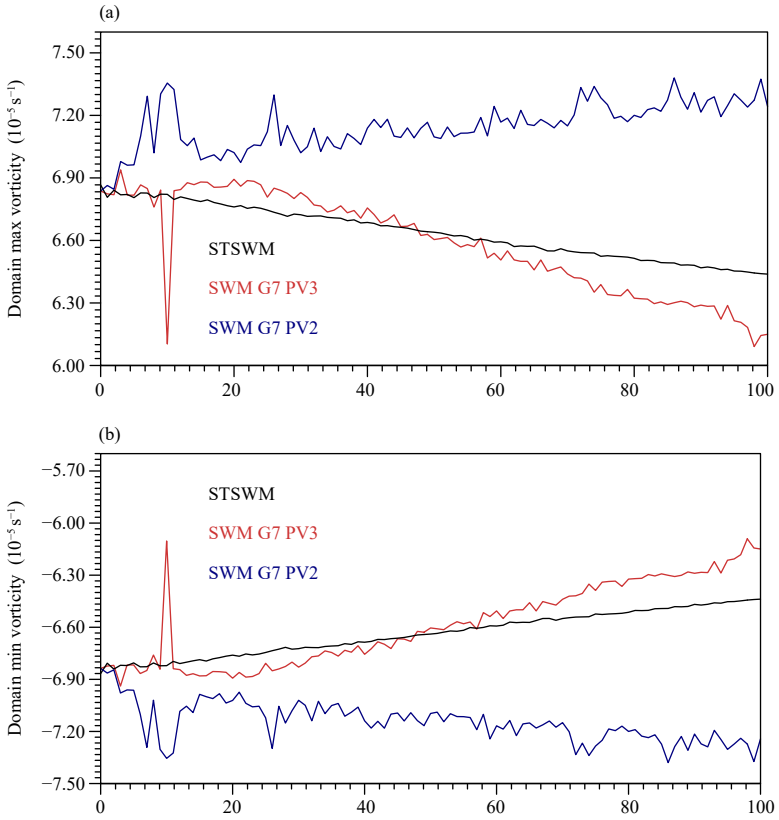

Fig. 15. (a) Maximum (max) and (b) minimum (min) values of vorticity from Days 0 to 100 in the domain from the STSWM (black line) and the icosahedral model with PV2 (blue line) and PV3 (red line) configured at G7.

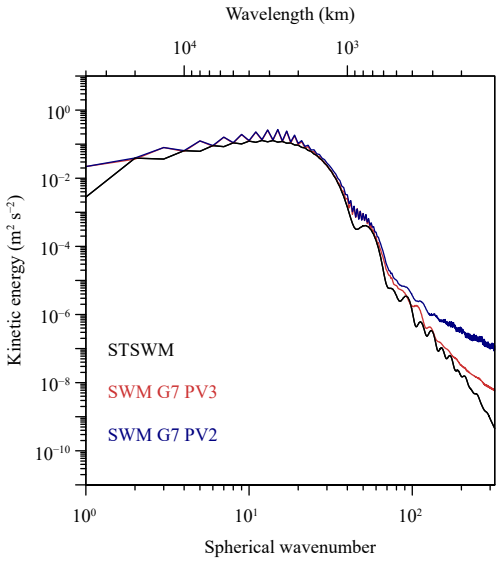

Fig. 16. Kinetic energy spectra averaged from Days 50 to 100 in the test case of colliding modons from the STSWM (black color) and the icosahedral model with PV2 (blue color) and PV3 (red color) configured at G7.

the reference model. As the resolution increases, the simulated kinetic spectra extend to smaller wavenumbers, closer to those in the reference model. The PV2 test tends to create a kinetic energy spectrum tail with a shallow slope as a result of the lack of damping. The icosahedral model maintains the symmetrical vorticity pattern and well simulates the propagation of the modon pairs. The modon amplitude decays over time with PV3 and increases over time with PV2. The kinetic energy spectra and the nonlinear spectral fluxes simulated by the grid-point model in colliding modons are roughly consistent with those simulated by the reference model.

4.2 *Discussion*

This study proposes a strategy to test the performance of a shallow water model on simulating the basic characteristics of atmospheric motion and vorticity dynamics. The kinetic energy spectra can be directly used to examine the performance of a barotropic shallow water model. The rotational and divergent components, and the stationary and transient components could be used to further examine the kinetic energy spectra, and be able to reveal key biases of kinetic energy spectra in terms of amplitude, trend or transition. The spectral fluxes could be used to test the mechanism of the slope characteristics of the kinetic energy spectra. The amplitude, propagation, collision, and kinetic energy characteristics of vor-

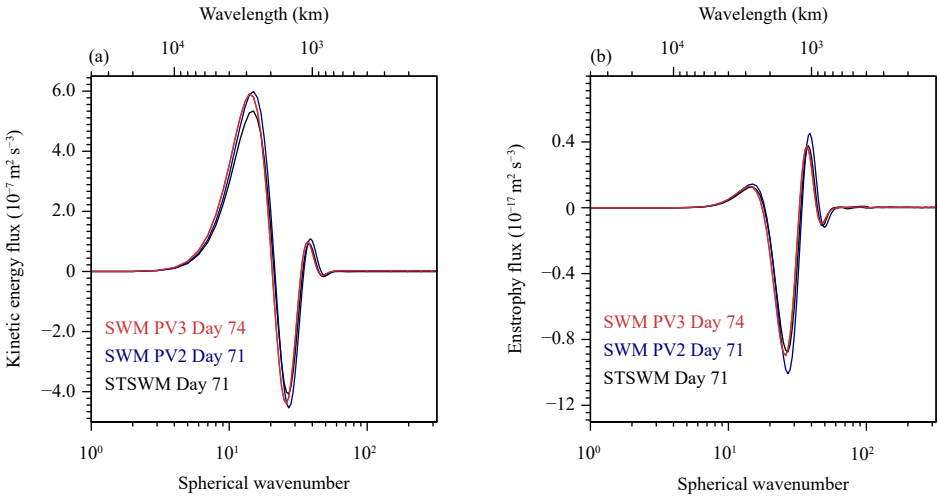

Fig. 17. (a) Rotational kinetic energy fluxes and (b) enstrophy fluxes in the test case of colliding modons from the STSWM on Day 71 (black color), the icosahedral model with PV2 (blue color) on Day 71, and the icosahedral model with PV3 on Day 74 (red color).

tices could be used to comprehensively test the model's performance on vorticity dynamics. Furthermore, the sensitivity of the model to different configurations (such as the resolution and PV flux operators as examined in this study) can also be revealed based on the kinetic spectra and colliding modons. Such sensitivity highlights the usefulness of these performance metrics in the context of a shallow water environment.

This study focuses on the shallow water environment. A natural question is that whether the model behavior in a shallow water environment has close relationship with that in the real atmosphere. For the kinetic energy spectrum shown in test case 6, the model exhibits a k^{-3} slope of the odd wavenumber, similar to the behavior of the large-scale motion in the real atmosphere. This feature can be maintained until higher wavenumbers as the resolution increases. This implies that the shallow water environment possesses certain similarity to the real atmospheric motions.

The interpolation from the unstructured grid to the Gaussian grid has some impacts on the kinetic energy spectra. Rípodas et al. (2009) suggested that the interpolation process limits the accuracy of spectra to ~10^{-8}. If the unstructured mesh values are interpolated to a Gaussian grid at a very high resolution, the kinetic energy spectra of the large wavenumbers exceeding the raw resolution will spuriously upwarp. Therefore, the resolution should not differ greatly during the interpolation procedure. In addition to the Inverse Distance Weighted Interpolation method used in this study, we also tested the nearest neighbor interpolation method. The differences in the kinetic spectra using two interpolation methods exhibit only at the large wavenumbers that exceed the raw resolution of the unstructured mesh, which does not affect the conclusions in this paper.

The kinetic energy spectrum evaluation method used in this study naturally applies to the global models because that spherical harmonic expansion requires periodic boundaries. The k^{-3} and $k^{-5/3}$ slope reference lines, and the kinetic energy spectrum derived from the Global Atmospheric Sampling Program (GASP) aircraft observations (Nastrom and Gage, 1985), and from the functional fit to the Measurement of Ozone by Airbus in-service aircraft (MOZAIC) observations (Lindborg, 1999) could be used as the reference solution to evaluate the real atmosphere. For the regional models that cannot use this method directly, a Fourier transform method after periodizing the meteorological fields by the preprocess of removing the tendency (Errico, 1985) or Discrete Cosine Transform (Denis et al., 2002) could be used for spectral decomposition of a two-dimensional field in a limited area case.

Acknowledgments. The authors are grateful to the three anonymous reviewers for their constructive comments.

Appendix: Computational Procedures of the Shallow Water Model

1. *Spatial discretization*

From a mathematical view, the shallow water equations contain the major horizontal operators of a three-dimensional model. The model may be separated to two modes: (1) the isolated transport mode, which can be used to examine the operators specifically associated

with the passive transport process; (2) the wave mode, which is the major physical mode for the barotropic shallow-water wave dynamics and is the focus of this study.

Based on the continuous-form equations and the definition of geometric location in the main text, a modified equation set that facilitates the numerical discretization may be written as follows:

$$\frac{\partial h_i}{\partial t} = -[\nabla \cdot F_e]_i, \tag{A1}$$

$$\frac{\partial u_e}{\partial t} = Q_e^{\perp} - \left[\frac{\partial}{\partial e}(\mathrm{g}(h_i + b_i) + K_i)\right]_e, \tag{A2}$$

where h_i is the thickness at the primal cell i, and u_e is the normal velocity at the edge of the primal cell. F_e is the normal thickness flux at the primal edge e; $Q_e^{\perp}$ is the nonlinear Coriolis term at the primal edge e. The superscript $\perp$ denotes the direction perpendicular to the unit normal vector of primal edge e ($\boldsymbol{n}_e$), and the direction follows $-\boldsymbol{k} \times \boldsymbol{n}_e$, where $\boldsymbol{k}$ is a unit vector along the local vertical direction. The variable b_i is the topographic height at primal cell i, K_i is the kinetic energy, g is the gravity parameter, and $\frac{\partial}{\partial e}$ denotes evaluating the gradient component along the normal direction of the primal edge. A concise summary of the major computational procedures is presented as follows, and a more comprehensive description of the basic operators is given by Ringler et al. (2010).

The right hand side of Eq. (A1) is approximated by using the divergence theorem:

$$[\nabla \cdot F_e]_i = \frac{1}{A_i} \sum\nolimits_{e \in \mathrm{EC}(i)} n_{e,i} F_e l_e, \tag{A3}$$

where A_i is the area of primal cell at i, l_e is the length of the primal edge. The spherical area of a polygon is evaluated by summing sub triangles that form it, and the spherical triangle area is evaluated based on the L' Huilier's Theorem (http://mathworld.wolfram.com/LHuiliersTheorem.html). The variable $e \in \mathrm{EC}(i)$ denotes all edges of primal cell i; $n_{e,i}$ is a binary indicator depending on the direction of $\boldsymbol{n}_e$, 1 for the outward direction relative to primal cell i and −1 for the inward direction; and $F_e = \hat{h}_e u_e$, where $\hat{h}_e$ is approximated by using the primal-cell flux operator:

$$\hat{h}_e = \mathrm{Flux}_{i \to e}(h_i). \tag{A4}$$

$\mathrm{Flux}_{i \to e}$ is a generic form, and its specific form depends on the target application. For the shallow-water wave-dynamics considered here, $\hat{h}_e = \left(\sum_{i \in \mathrm{CE}(e)} h_i\right)/2$, where $i \in \mathrm{CE}(e)$ denotes two neighboring primal cells that share edge e, i.e., a two-point average is used, which is crucial for an energy-conserving shallow-water discretization. When $F_e = u_e$, Eq. (A3) diagnoses the divergence.

The nonlinear Coriolis term (NCT) is given by

$$Q_e^{\perp} = -\frac{1}{d_e} \sum\nolimits_{e' \in \mathrm{ECP}(e)} [w_{e,e'} l_{e'} F_{e'} \tilde{q}_{e,e'}], \tag{A5}$$

where d_e is the length of dual edge, $e' \in \mathrm{ECP}(e)$ denotes all edges of two neighboring primal cells that share edge e, and $w_{e,e'}$ is the vector remapping weight following Thuburn et al. (2009):

$$w_{e,e'} = \left[\left(\sum\nolimits_{v=v_1}^{v=v_2} \frac{A_{iv}}{A_i}\right) - 0.5\right] n_{e'i} t_{e,v_2}, \tag{A6}$$

where A_{iv} is a kite-shape intersecting area between primal cell i and dual cell v; $t_{e,v}$ is a binary indicator depending on the direction of $\boldsymbol{k} \times \boldsymbol{n}_e$, 1 for the inward direction relative to dual cell v and −1 for the outward direction; $\sum_{v=v_1}^{v=v_2} \frac{A_{iv}}{A_i}$ means a traversal sum from edge e' to edge e, the first dual cell encountered is v_1, and the last dual cell encountered is v_2: sum A_{iv}/A_i associated with each dual cell from v_1 to v_2; and the final $w_{e,e'}$ is corrected with the sign corrector $n_{e'i} t_{e,v_2}$ to obtain a correct sign. If $e' = e$, $w_{e,e'} = 0$.

The variable $\tilde{q}_{e,e'}$ is evaluated as $\tilde{q}_{e,e'} = (\tilde{q}_e + \tilde{q}_{e'})/2$ or $\tilde{q}_{e,e'} = \tilde{q}_e$. Following Zhang et al. (2019), the first one is referred to as $\mathrm{NCT}_{\mathrm{non\_local}}$ as it brings PV information from e' to e, while the second one is referred to as $\mathrm{NCT}_{\mathrm{local}}$ because only local PV information at e is used. The variable $\tilde{q}_e$ is evaluated based on the dual-cell flux operator:

$$\tilde{q}_e = \mathrm{Flux}_{v \to e}(q_v), \tag{A7}$$

and its specific form is given later. The variable $q_v = \eta_v / h_v$, η_v is the absolute vorticity defined at the dual cell, and h_v is the remapped fluid thickness at the dual cell:

$$\eta_v = f + \boldsymbol{k} \cdot (\nabla \times \boldsymbol{V})_v = f + \frac{1}{A_v} \sum\nolimits_{e \in \mathrm{EV}(v)} t_{e,v} u_e d_e, \tag{A8}$$

$$h_v = \frac{1}{A_v} \sum\nolimits_{i \in \mathrm{CV}(v)} A_{iv} h_i, \tag{A9}$$

where f is the Coriolis parameter, A_v is the area of dual cell v, $e \in \mathrm{EV}(v)$ denotes all edges of dual cell v, $i \in \mathrm{CV}(v)$ denotes primal cells that form the vertex of dual cell v. Finally, the kinetic energy K_i is given by $K_i = \frac{1}{A_i} \sum_{e \in \mathrm{EC}(i)} \frac{l_e d_e}{4} u_e^2$, and the gradient component along the normal direction of primal edge e reads $\frac{\partial}{\partial e} = \frac{1}{d_e} \sum_{i \in \mathrm{CE}(e)} -n_{e,i} h_i$.

This horizontal discretization has many desirable properties for geophysical fluid modeling. A limitation is that the basic operators (e.g., divergence, gradient, and vector reconstruction) possess a low order of accuracy,

although the flux operator can be made with high-order approximation. For example, the discrete divergence operator is nominally second-order accurate for a regular hexagon. For the isolated transport solver, in solid body rotation transport of a continuous Gaussian hill [Williamson et al. (1992)'s test case 1 but with a continuous Gaussian hill given by $h = 1000 \exp(-3\pi^2 r^2)$, where r is the angular distance in radians from the hill center located at the equator], several flux operators in the model exhibit third-order convergence in unlimited and limited tests, except that the l_∞ norm in the limited test exhibits second-order convergence (Fig. A1). For deformational flow transport of two Gaussian hills that may challenge the pentagon of the icosahedral grid, the solution exhibits second-order convergence due to the influence of mesh irregularity (cf., Zhang, 2018), and the convergence rate is also sensitive to the Courant number. For the shallow water wave mode considered in this study, some basic operators may be inconsistent under certain mesh configurations (cf., Thuburn et al., 2014; Peixoto, 2016), but the SCVT optimization is generally helpful. This issue has led to a non-convergence behavior of the l_∞ error norm in the zonal balanced flow test (Ringler et al., 2010; Zhang, 2018), a problem that was also found in some other quasi-uniform grid models based on the staggering finite-volume methods (e.g., Harris and Lin, 2012). For more complex real-world flow, this issue seems to be less evident (e.g., Ji, 2016), and its realistic implications remain explored. Also note that the l_∞ norm in the zonal flow test will exhibit second-order convergence if one adopts the model-generated state (e.g., Day 1 or Day 2 solution) as the initial condition (Fig. A2).

2. *Time integrator*

The shallow water framework contains several time integrators. For results shown here, a three-stage third-or-

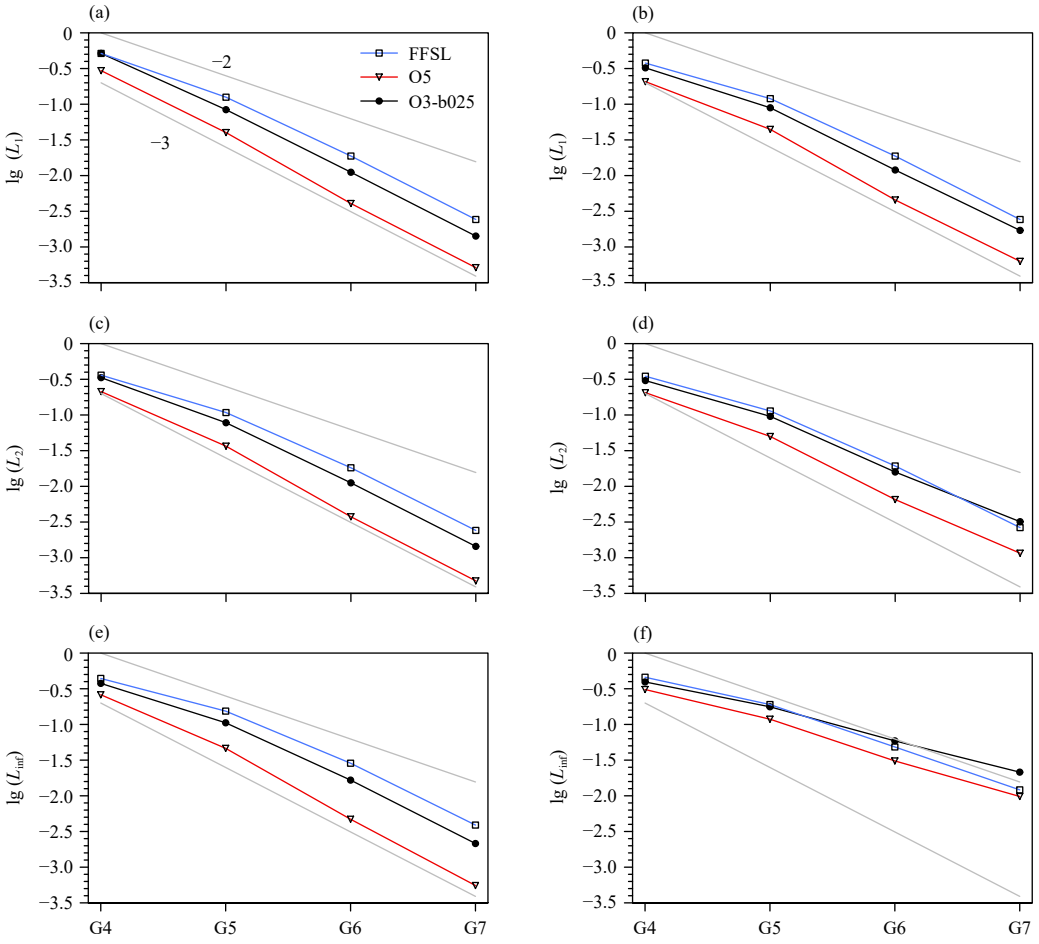

Fig. A1. Solid body rotation transport of a Gaussian hill: (a, b) l_1, (c, d) l_2, and (e, f) l_∞ error norms (denoted by L_1, L_2, and L_{inf}, respectively) at grid levels G4–G7 from the (a, c, e) unlimited and (b, d, f) limited tests. Three flux operators are examined, including a nominal third-order operator with a dissipation coefficient 0.25 (O3-b025; black line), a nominal fifth-order operator with a dissipation coefficient 1 (O5; red line), and an incremental remapping style flux-form semi-Lagrangian (FFSL; blue line) scheme. The upper and lower gray lines denote the ideal second-order (−2) and third-order (−3) convergence lines, respectively. For more details regarding the numerical methods, see Zhang et al. (2019).

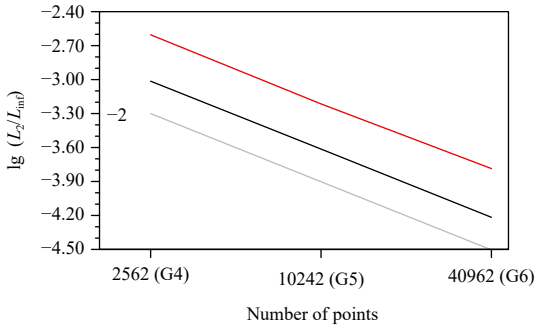

Fig. A2. Solution errors of the thickness field against the number of points at the grid levels G4–G6 in Williamson et al. (1992)'s test case 2 (zonal flow test with PV3). The black line denotes the l_2 error norm (L_2), and the red line denotes the l_∞ error norm (L_{inf}), both of which exhibit second-order convergence (−2; denoted by the gray line) when comparing the difference between solutions on Day 13 and Day 1. See Zhang (2018) for more details regarding the test case setup.

der Runge–Kutta method (Wicker and Skamarock, 2002) is used:

$$\begin{aligned}\mathcal{H}^* &= \mathcal{H}^n + \frac{\Delta t}{3} F(\mathcal{H}^n);\\ \mathcal{H}^{**} &= \mathcal{H}^n + \frac{\Delta t}{2} F(\mathcal{H}^*);\\ \mathcal{H}^{n+1} &= \mathcal{H}^n + \Delta t F(\mathcal{H}^{**}),\end{aligned} \tag{A10}$$

where $\mathcal{H}$ denotes a generic variable, n and $n + 1$ denote two time levels, * and ** denote intermediate time levels, and $F(\mathcal{H})$ denotes evaluating spatial tendency.

3. *PV flux operators*

The PV transport process is important for atmospheric circulation (Hoskins et al., 1985), and the representation of the PV transport process affects the behavior of the model (Sadourny and Basdevant, 1985; Lin and Rood, 1997; Weller, 2012). The PV flux operator in Eq. (A7) determines how $\tilde{q}_e$ is evaluated based on q_v. In the present work, we evaluate two choices. The first one is simply a two-point average, and is referred to as PV2:

$$\tilde{q}_e = \frac{1}{2}\left(q_{v_1} + q_{v_2}\right), \tag{A11}$$

where q_{v1} and q_{v2} are PV values associated with two dual cells. The second one is based on a high-order flux reconstruction (Skamarock and Gassmann, 2011; Zhang, 2018), and is referred to as PV3:

$$\begin{aligned}\tilde{q}_e = &\frac{1}{2}\left(q_{v_1} + q_{v_2}\right) - \frac{1}{12}\left(\delta^2 q_{v_1} + \delta^2 q_{v_2}\right)\\ &+ \frac{\beta}{12} n_{e,v_1v_2}\left(\delta^2 q_{v_2} - \delta^2 q_{v_1}\right),\end{aligned} \tag{A12}$$

where $\delta^2 q_v = {d_e}^2\left(\frac{\partial^2 q}{\partial e^2}\right)_v$, $\left(\frac{\partial^2 q}{\partial e^2}\right)_v$ is evaluated at the dual cell based on a quadratic polynomial reconstruction. n_{e,v_1v_2} is a binary indicator depending on the direction of the reconstructed tangent velocity relative to v_1v_2: 1 for the same direction and −1 for the opposite direction. The variable β ranges from 0 to 1 and controls the strength of an implicit numerical diffusion term. If Eq. (A12) is used in a symmetric way (e.g., flux difference), the β term will lead to a fourth-order hyper-diffusion term with a hyper-viscosity proportional to the Courant number. Meanwhile, because the purely upwind PV3 configuration (β = 1) is used, Eq. (A12) may be rewritten as:

$$\tilde{q}_e = \frac{1}{2}\left(q_{v_1} + q_{v_2}\right) - \frac{1}{6}\delta^2 q_{v\_\text{upwind}}. \tag{A13}$$

The implicit diffusion term $\frac{\partial^2 q}{\partial e^2}$ helps to smooth small-scale structures, and also provides a more accurate flux approximation. PV3 does not increase the communication region of the model (2 halo layers are used).

REFERENCES

Boer, G. J., and T. G. Shepherd, 1983: Large-scale two-dimensional turbulence in the atmosphere. *J. Atmos. Sci.*, **40**, 164–184, doi: 10.1175/1520-0469(1983)040<0164:LSTDTI>2.0.CO;2.

Burgess, A. B. H., A. R. Erler, and T. G. Shepherd, 2013: The troposphere-to-stratosphere transition in kinetic energy spectra and nonlinear spectral fluxes as seen in ECMWF analyses. *J. Atmos. Sci.*, **70**, 669–687, doi: 10.1175/JAS-D-12-0129.1.

Charney, J. G., 1971: Geostrophic turbulence. *J. Atmos. Sci.*, **28**, 1087–1095, doi: 10.1175/1520-0469(1971)028<1087:GT>2.0.CO;2.

Chen, X., S.-J. Lin, and L. M. Harris, 2018: Towards an unstaggered finite-volume dynamical core with a fast Riemann solver: 1-D linearized analysis of dissipation, dispersion, and noise control. *J. Adv. Model. Earth Syst.*, **10**, 2333–2356, doi: 10.1029/2018MS001361.

Denis, B. J., J. Côté, and R. Laprise, 2002: Spectral decomposition of two-dimensional atmospheric fields on limited-area domains using the Discrete Cosine Transform (DCT). *Mon. Wea. Rev.*, **130**, 1812–1829, doi: 10.1175/1520-0493(2002)130<1812:SDOTDA>2.0.CO;2.

Errico, R. M., 1985: Spectra computed from a limited area grid. *Mon. Wea. Rev.*, **113**, 1554–1562, doi: 10.1175/1520-0493(1985)113<1554:SCFALA>2.0.CO;2.

Falkovich, G., 1992: Inverse cascade and wave condensate in mesoscale atmospheric turbulence. *Phys. Rev. Lett.*, **69**, 3173–3176, doi: 10.1103/PhysRevLett.69.3173.

Gage, K. S., and G. D. Nastrom, 1986: Theoretical interpretation of atmospheric wavenumber spectra of wind and temperature observed by commercial aircraft during GASP. *J. Atmos. Sci.*, **43**, 729–740, doi: 10.1175/1520-0469(1986)043<0729:TIOAWS>2.0.CO;2.

Gassmann, A., 2011: Inspection of hexagonal and triangular C-grid discretizations of the shallow water equations. *J. Comput. Phys.*, **230**, 2706–2721, doi: 10.1016/j.jcp.2011.01.014.

Hack, J. J., and R. Jakob, 1992: Description of A Global Shallow Water Model Based on the Spectral Transform Method. NCAR TECHNICAL NOTE, NCAR/TN-343+STR, National Center for Atmospheric Research, Boulder, Colorado, 39 pp.

Harris, L. M., and S.-J. Lin, 2012: A two-way nested global–regional dynamical core on the cubed-sphere grid. *Mon. Wea. Rev.*, **141**, 283–306, doi: 10.1175/MWR-D-11-00201.1.

Heikes, R., and D. A. Randall, 1995: Numerical integration of the shallow-water equations on a twisted icosahedral grid. Part I: Basic design and results of tests. *Mon. Wea. Rev.*, **123**, 1862–1880, doi: 10.1175/1520-0493(1995)123<1862:NIOTSW>2.0.CO;2.

Hoskins, B. J., 1973: Stability of the Rossby–Haurwitz wave. *Quart. J. Roy. Meteor. Soc.*, **99**, 723–745, doi: 10.1002/qj.49709942213.

Hoskins, B. J., M. E. McIntyre, and A. W. Robertson, 1985: On the use and significance of isentropic potential vorticity maps. *Quart. J. Roy. Meteor. Soc.*, **111**, 877–946, doi: 10.1002/qj.49711147002.

Jacobsen, D. W., M. Gunzburger, T. Ringler, et al., 2013: Parallel algorithms for planar and spherical Delaunay construction with an application to centroidal Voronoi tessellations. *Geosci. Model Dev.*, **6**, 1353–1365, doi: 10.5194/gmd-6-1353-2013.

Jakob-Chien, R., J. J. Hack, and D. L. Williamson, 1995: Spectral transform solutions to the shallow water test set. *J. Comput. Phys.*, **119**, 164–187, doi: 10.1006/jcph.1995.1125.

Ji, M., 2016: Dynamical core evaluation test report for NOAA's next generation global prediction system (NGGPS). https://www.weather.gov/media/sti/nggps/NGGPS%20Dycore%20Phase%202%20Test%20Report%20website.pdf. [Accessing date: December 8, 2017].

Kolmogorov, A. N., 1991: The local structure of turbulence in incompressible viscous fluid for very large Reynolds number. *Proc. Roy. Soc. A Mathem. Phys. Eng. Sci.*, **434**, 9–13, doi: 10.1098/rspa.1991.0075.

Koshyk, J. N., and K. Hamilton, 2001: The horizontal kinetic energy spectrum and spectral budget simulated by a high-resolution troposphere–stratosphere–mesosphere GCM. *J. Atmos. Sci.*, **58**, 329–348, doi: 10.1175/1520-0469(2001)058<0329:THKESA>2.0.CO;2.

Koshyk, J. N., B. A. Boville, K. Hamilton, et al., 1999: Kinetic energy spectrum of horizontal motions in middle-atmosphere models. *J. Geophys. Res. Atmos.*, **104**, 27177–27190, doi: 10.1029/1999JD900814.

Lilly, D. K., 1983: Stratified turbulence and the mesoscale variability of the atmosphere. *J. Atmos. Sci.*, **40**, 749–761, doi: 10.1175/1520-0469(1983)040<0749:STATMV>2.0.CO;2.

Lin, S. J., and R. B. Rood, 1997: An explicit flux-form semi-lagrangian shallow-water model on the sphere. *Quart. J. Roy. Meteor. Soc.*, **123**, 2477–2498, doi: 10.1002/qj.49712354416.

Lin, S. J., L. Harris, X. Chen, et al., 2017: Colliding modons: A nonlinear test for the evaluation of global dynamical cores. *J. Adv. Model. Earth Syst.*, **9**, 2483–2492, doi: 10.1002/2017MS000965.

Lindborg, E., 1999: Can the atmospheric kinetic energy spectrum be explained by two-dimensional turbulence? *J. Fluid Mech.*, **388**, 259–288, doi: 10.1017/S0022112099004851.

Lindborg, E., 2006: The energy cascade in a strongly stratified fluid. *J. Fluid Mech.*, **550**, 207–242, doi: 10.1017/S0022112005008128.

Nastrom, G. D., K. S. Gage, 1985: A climatology of atmospheric wavenumber spectra of wind and temperature observed by commercial aircraft. *J. Atmos. Sci.*, **42**, 950–960, doi: 10.1175/1520-0469(1985)042<0950:ACOAWS>2.0.CO;2.

Nastrom, G. D., K. S. Gage, and W. H. Jasperson, 1984: Kinetic energy spectrum of large- and mesoscale atmospheric processes. *Nature*, **310**, 36–38, doi: 10.1038/310036a0.

Palmer, T. N., 2001: A nonlinear dynamical perspective on model error: A proposal for non-local stochastic–dynamic parametrization in weather and climate prediction models. *Quart. J. Roy. Meteor. Soc.*, **127**, 279–304, doi: 10.1002/qj.49712757202.

Palmer, T. N., G. J. Shutts, R. Hagedorn, et al., 2005: Representing model uncertainty in weather and climate prediction. *Annu. Rev. Earth Planet. Sci.*, **33**, 163–193, doi: 10.1146/annurev.earth.33.092203.122552.

Peixoto, P. S., 2016: Accuracy analysis of mimetic finite volume operators on geodesic grids and a consistent alternative. *J. Comput. Phys.*, **310**, 127–160, doi: 10.1016/j.jcp.2015.12.058.

Randall, D. A., 1994: Geostrophic adjustment and the finite-difference shallow-water equations. *Mon. Wea. Rev.*, **122**, 1371–1377, doi: 10.1175/1520-0493(1994)122<1371:GAATFD>2.0.CO;2.

Ringler, T., L. L. Ju, and M. Gunzburger, 2008: A multiresolution method for climate system modeling: Application of spherical centroidal Voronoi tessellations. *Ocean Dyn.*, **58**, 475–498, doi: 10.1007/s10236-008-0157-2.

Ringler, T. D., J. Thuburn, J. B. Klemp, et al., 2010: A unified approach to energy conservation and potential vorticity dynamics for arbitrarily-structured C-grids. *J. Comput. Phys.*, **229**, 3065–3090, doi: 10.1016/j.jcp.2009.12.007.

Rípodas, P., A. Gassmann, J. Förstner, et al., 2009: Icosahedral shallow water model (ICOSWM): Results of shallow water test cases and sensitivity to model parameters. *Geosci. Model Dev.*, **2**, 231–251, doi: 10.5194/gmd-2-231-2009.

Sadourny, R., and C. Basdevant, 1985: Parameterization of subgrid scale barotropic and baroclinic eddies in quasi-geostrophic models: Anticipated potential vorticity method. *J. Atmos. Sci.*, **42**, 1353–1363, doi: 10.1175/1520-0469(1985)042<1353:POSSBA>2.0.CO;2.

Saujani, S., and T. G. Shepherd, 2006: A unified theory of balance in the extratropics. *J. Fluid Mech.*, **569**, 447–464, doi: 10.1017/S0022112006002783.

Shutts, G., 2005: A kinetic energy backscatter algorithm for use in ensemble prediction systems. *Quart. J. Roy. Meteor. Soc.*, **131**, 3079–3102, doi: 10.1256/qj.04.106.

Skamarock, W. C., 2004: Evaluating mesoscale NWP models using kinetic energy spectra. *Mon. Wea. Rev.*, **132**, 3019–3032, doi: 10.1175/MWR2830.1.

Skamarock, W. C., and A. Gassmann, 2011: Conservative transport schemes for spherical geodesic grids: High-order flux operators for ODE-based time integration. *Mon. Wea. Rev.*, **139**, 2962–2975, doi: 10.1175/MWR-D-10-05056.1.

Thuburn, J., and Y. Li, 2000: Numerical simulations of Rossby–Haurwitz waves. *Tellus A: Dyn. Meteor. Oceanogr.*, **52**, 181–189, doi: 10.3402/tellusa.v52i2.12258.

Thuburn, J., T. D. Ringler, W. C. Skamarock, et al., 2009: Numer-

ical representation of geostrophic modes on arbitrarily structured C-grids. *J. Comput. Phys.*, **228**, 8321–8335, doi: 10.1016/j.jcp.2009.08.006.

Thuburn, J., C. J. Cotter, and T. Dubos, 2014: A mimetic, semi-implicit, forward-in-time, finite volume shallow water model: Comparison of hexagonal–icosahedral and cubed-sphere grids. *Geosci. Model Dev.*, **7**, 909–929, doi: 10.5194/gmd-7-909-2014.

Trenberth, K. E., and A. Solomon, 1993: Implications of global atmospheric spatial spectra for processing and displaying data. *J. Climate*, **6**, 531–545, doi: 10.1175/1520-0442(1993)006<0531:IOGASS>2.0.CO;2.

Weller, H., 2012: Controlling the computational modes of the arbitrarily structured C grid. *Mon. Wea. Rev.*, **140**, 3220–3234, doi: 10.1175/MWR-D-11-00221.1.

Wicker, L. J., and W. C. Skamarock, 2002: Time-splitting methods for elastic models using forward time schemes. *Mon. Wea. Rev.*, **130**, 2088–2097, doi: 10.1175/1520-0493(2002)130<2088:TSMFEM>2.0.CO;2.

Williamson, D. L., J. B. Drake, J. J. Hack, et al., 1992: A standard test set for numerical approximations to the shallow water equations in spherical geometry. *J. Comput. Phys.*, **102**, 211–224, doi: 10.1016/S0021-9991(05)80016-6.

Zhang, Y., 2018: Extending high-order flux operators on spherical icosahedral grids and their applications in the framework of a shallow water model. *J. Adv. Model. Earth Syst.*, **10**, 145–164, doi: 10.1002/2017MS001088.

Zhang, Y., J. Li, R. C. Yu, et al., 2019: A layer-averaged nonhydrostatic dynamical framework on an unstructured mesh for global and regional atmospheric modeling: Model description, baseline evaluation, and sensitivity exploration. *J. Adv. Model. Earth Syst.*, **11**, 1685–1714, doi: 10.1029/2018MS001539.

Tech & Copy Editor: Hongqun ZHANG